Chemical Science

ROYAL SOCIETY OF CHEMISTRY

EDGE ARTICLE

View Article Online
View Journal | View Issue

Cite this: *Chem. Sci.*, 2025, **16**, 9484

All publication charges for this article have been paid for by the Royal Society of Chemistry

Nanostructured amorphous Ni–Co–Fe phosphide as a versatile electrocatalyst towards seawater splitting and aqueous zinc–air batteries†

Masumeh Moloudi, [a] Abolhassan Noori, *[a] Mohammad S. Rahmanifar, [b] Maher F. El-Kady, [c] Ebrahim Mousali, [a] Nahla B. Mohamed, [cd] Xinhui Xia, [ef] Yongqi Zhang, [g] Ajayan Vinu, [h] Mewin Vincent, [i] Damian Kowalski, [i] Richard B. Kaner *[cj] and Mir F. Mousavi *[a]

Electrocatalysis provides a desirable approach for moving toward a sustainable energy future. Herein, a rapid and facile potential pulse method was implemented for a one-pot electrosynthesis of the amorphous Ni–Co–Fe–P (NCFP) electrocatalyst. The 2 mg cm^{-2} loaded electrode displayed excellent trifunctional electrocatalytic activities toward the hydrogen evolution reaction ($\eta_{j=10}^{HER}$ = 102 mV), oxygen evolution reaction ($\eta_{j=10}^{OER}$ = 250 mV), and oxygen reduction reaction ($E_{1/2}^{ORR}$ = 0.73 V) in alkaline solutions. Interestingly, even a lower overpotential of $\eta_{j=10}^{HER}$ = 86 mV was obtained at a super-high mass loading of 18.7 mg cm^{-2}, demonstrating its feasibility for industrial-level applications. The NCFP electrocatalyst also offered superior catalytic activity in alkaline seawater electrolysis at industrially required current rates (500 mA cm^{-2}). When implemented as an air cathode catalyst of an aqueous and quasi-solid state zinc–air battery, both devices delivered excellent performance. This study provides insights into a transformative technology towards a sustainable energy future.

Received 17th February 2025
Accepted 20th April 2025

DOI: 10.1039/d5sc01249j

rsc.li/chemical-science

Introduction

Since fossil fuels are by far the largest contributor to environmental deterioration and climate change, ending our reliance on fossil fuels and investing in clean and renewable energy sources is becoming increasingly urgent. Hydrogen has the potential to be a game-changer in fostering a more sustainable future because of its intrinsically high energy density (~282 kJ mol^{-1}), environmentally benign nature, light weight, and near-zero carbon emissions.[1] However, hydrogen production by electrochemical water splitting, depends on highly effective electrocatalysts to minimize the overpotentials for the hydrogen evolution reaction (HER) and the oxygen evolution reaction (OER).[2,3] Given that freshwater is scarce (3.5% of the total), splitting seawater is a critical step towards a viable hydrogen industry, with the added benefit of producing fresh drinking water.[4–6] On the other hand, metal–air batteries have also been explored as clean energy carriers, wherein the OER and oxygen reduction reaction (ORR) are key electrocatalytic processes.[7–11] Thus, tailoring advanced materials based on non-noble-transition metals[12–14] as either mono-, bi-, or multi-functional electrocatalysts towards the HER, OER, and ORR has been a hot topic.[15–18] Amorphous materials have opened their place among the HER, OER, and ORR electrocatalysts and have even surpassed their crystalline counterparts.[19,20] This catalytic activity enhancement can be ascribed to several key parameters including a larger electrochemically active surface area (ECSA), efficient ion transport, flexibility, self-healing and self-reconstruction capabilities due to their disordered atomic structure that enables them to redistribute stress and recover from damage, abundant catalytically active defect sites or

[a]Department of Chemistry, Faculty of Basic Sciences, Tarbiat Modares University, Tehran 14117-13116, Iran. E-mail: noori@modares.ac.ir; mousavim@modares.ac.ir
[b]Faculty of Basic Sciences, Shahed University, Tehran 3319118-651, Iran
[c]Department of Chemistry and Biochemistry, California NanoSystems Institute, University of California, Los Angeles (UCLA), CA 90095, USA. E-mail: kaner@chem.ucla.edu
[d]Chemistry Department, Faculty of Science, Cairo University, Giza, 12613, Egypt
[e]College of Materials Science & Engineering, Zhejiang University of Technology, Hangzhou 310014, China
[f]State Key Laboratory of Silicon Materials, Key Laboratory of Advanced Materials and Applications for Batteries of Zhejiang Province, School of Materials Science & Engineering, Zhejiang University, Hangzhou 310027, China
[g]Institute of Fundamental and Frontier Science, University of Electronic Science and Technology of China, Chengdu 611371, China
[h]Global Innovative Centre for Advanced Nanomaterials, The School of Engineering, College of Engineering, Science and Environment, The University of Newcastle, Callaghan 2308, Australia
[i]Faculty of Chemistry, University of Warsaw, 02-093 Warsaw, Poland
[j]Department of Materials Science and Engineering, University of California, Los Angeles (UCLA), CA 90095, USA. E-mail: kaner@chem.ucla.edu

† Electronic supplementary information (ESI) available: Experimental procedures; characterization of the samples; electrochemical studies in 3E and 2E cell setups; comparison tables, calculation formula, optimization steps, ESI videos. See DOI: https://doi.org/10.1039/d5sc01249j

dangling bonds, and the possibility to be tailored in an optimal elemental ratio with the desired catalytic performance.[21–23] Transition metal phosphides (TMP), with the merits of abundant resources, tunable composition, and high electrical conductivity, have been explored as attractive electrocatalysts.[24,25] The higher electronegativity of phosphorus induces electron delocalization, forming partially positively charged metals and negatively charged phosphorus ($M^{\delta+}$–$P^{\delta-}$).[26,27] This electronic structure closely resembles the active site of hydrogenase, wherein metals function as hydride (H^-) acceptors and phosphorus serves as proton (H^+) acceptors, essential for the HER/OER/ORR processes.[28] Phosphorus also enables fine-tuning of the band gap and increases the density of states near the Fermi level, ensuring an abundance of charge carriers, akin to noble metals, which is critical for efficient electrocatalytic processes.[29] Moreover, the covalent nature of the M–P bonds contributes to exceptional long-term stability of TMPs, while the coexistence of metallic M–M bonds with non-metallic M–P and P–P bonds imparts high chemical stability and mechanical durability. This unique bonding framework also facilitates compositional versatility, allowing TMPs (M_xP_y) to span a broad range of stoichiometric configurations with different $x:y$ ratios.[30,31] Such structural and electronic synergies underline the immense potential of TMPs in advancing next-generation electrocatalysts.[32] However, developing multi-elemental electrocatalysts is an effective approach owing to the synergistic interplay among the different elements and modulation of the electronic properties of the catalysts for energy-efficient adsorption of reaction intermediates.[33,34] Although multi-elemental electrocatalysts have demonstrated efficient catalytic activity for the HER or OER, few have shown bifunctional activities towards both the HER and OER in the same electrolyte. Note also that noble metal-based OER and HER electrocatalysts rarely show any bifunctionality.[35] In addition, most of the synthetic strategies reported thus far suffer from intricacy, high cost, inadequate scalability, undesired by-products, and environmental concerns.

Herein, a facile, green, and one-pot electrosynthesis method is reported for the preparation of an amorphous Ni–Co–Fe–P (NCFP) electrocatalyst using NaH_2PO_2 as a green phosphorus source (Fig. 1). The chemical compositions, morphology, and thickness of the electrocatalyst film were tailored *via* real-time tuning of the potential pulse parameters. The trifunctional NCFP electrocatalyst displayed excellent catalytic activities towards the HER, the OER, and the ORR, with superb applications for overall water/seawater splitting and zinc–air batteries.

Experimental section

Materials

$NiCl_2 \cdot 6H_2O$ (>98%), $CoCl_2 \cdot 6H_2O$ (>98%), $FeCl_3 \cdot 6H_2O$ (>98%), $NaH_2PO_2 \cdot H_2O$ (99%), CH_3COONa (99%), HCl (>37%), KOH (>99%), KCl (>99%), NaCl (>99%), ethanol (>99%), zinc coarse powder with a particle size in the range from 0.3–1.5 mm (14–50 mesh ASTM), and RuO_2 were obtained from Merck (Germany). Poly(vinyl alcohol) (PVA, MW = 72 000), Nafion solution (5 wt%), PTFE solution (60 wt%) and Pt/C catalyst (20 wt%, with an average particle size of ≤5.0 nm, loaded on graphitized carbon) were purchased from Sigma-Aldrich (USA). Zinc foil (0.1 mm, 99.9% purity) and nickel foam (0.27 mm) were obtained from a local market. Seawater was collected from the Caspian Sea in Iran. All other chemicals were of analytical reagent grade and used without further purification. All aqueous solutions were prepared with doubly distilled water.

Instrumentation

The crystal structures of the as-prepared catalysts were obtained using a powder X-ray diffractometer (XRD, Philips X'Pert MPD X-ray diffractometer with Cu Kα radiation, $\lambda = 1.5406$ Å, generated at 40 kV and 40 mA with a step size of $0.02° \ s^{-1}$). XRD spectra were analyzed using Xpert software. X-ray photoelectron spectroscopy (XPS) measurements of the samples were recorded using an X-ray photoelectron spectroscope (Specs model EA10 plus, Bestec Co, Germany), with Al Kα radiation (15 kV). All XPS spectra were calibrated based on the C 1s photoemission peak at 284.8 eV as a reference and analyzed by Casa XPS software. The surface morphology and topological features of the materials were characterized using a field emission scanning electron microscope (FE-SEM, Philips) and a high-resolution transmission electron microscope (HR-TEM, FEI Tecnai F20). For structural investigation of the materials, fast Fourier-transform (FFT) and selected area electron diffraction (SAED) patterns were obtained from the HR-TEM images. The compositional distribution of the elements was investigated using a high-angle annular dark-field scanning transmission electron microscopy (HAADF-STEM) mode of an FEI Tecnai G2 F20 Super Twin microscope and also using an energy dispersive X-ray spectrometer (EDS, as an attachment to an SEM instrument). The *ex situ* Raman spectra of the pristine electrode and the *in situ* Raman spectra of the electrode were collected at selected potentials under HER/OER conditions using a Thermo Scientific DXR3 Raman microscope fitted with a 532 nm laser. The laser power was maintained at 3 mW for OER and 1 mW for HER reaction for the maximum clarity of the spectrum in the respective systems. Measurements were carried out with a 10× objective with a 0.25 numerical Olympus aperture. Collected Raman spectra were subjected to fluorescence background correction for better resolution of the Raman bands. Measurements were repeated three times at three different electrode spots to ensure reproducibility. The Fourier transform infrared (FT-IR) spectra of the samples were obtained using a NICOLET FT-IR 100 spectrometer with KBr pellets. The X-ray absorption fine structure (XAFS) investigations were carried out at the energy scanning EXAFS beamline (BL-9) of the Indus-2 Synchrotron source (2.5 GeV, 300 mA) at the Raja Ramanna Centre for Advanced Technology (RRCAT), Indore, India at room temperature. The EXAFS data were converted and normalized into *K*-space and *R*-space using the Athena software, following established protocols.[36]

The electrochemical studies were conducted using a Bio-Logic SP-300 potentiostat/galvanostat (BioLogic, France) controlled *via* EC-Lab v11.36 software. Electrochemical characterization of the electrocatalysts was evaluated in a three-

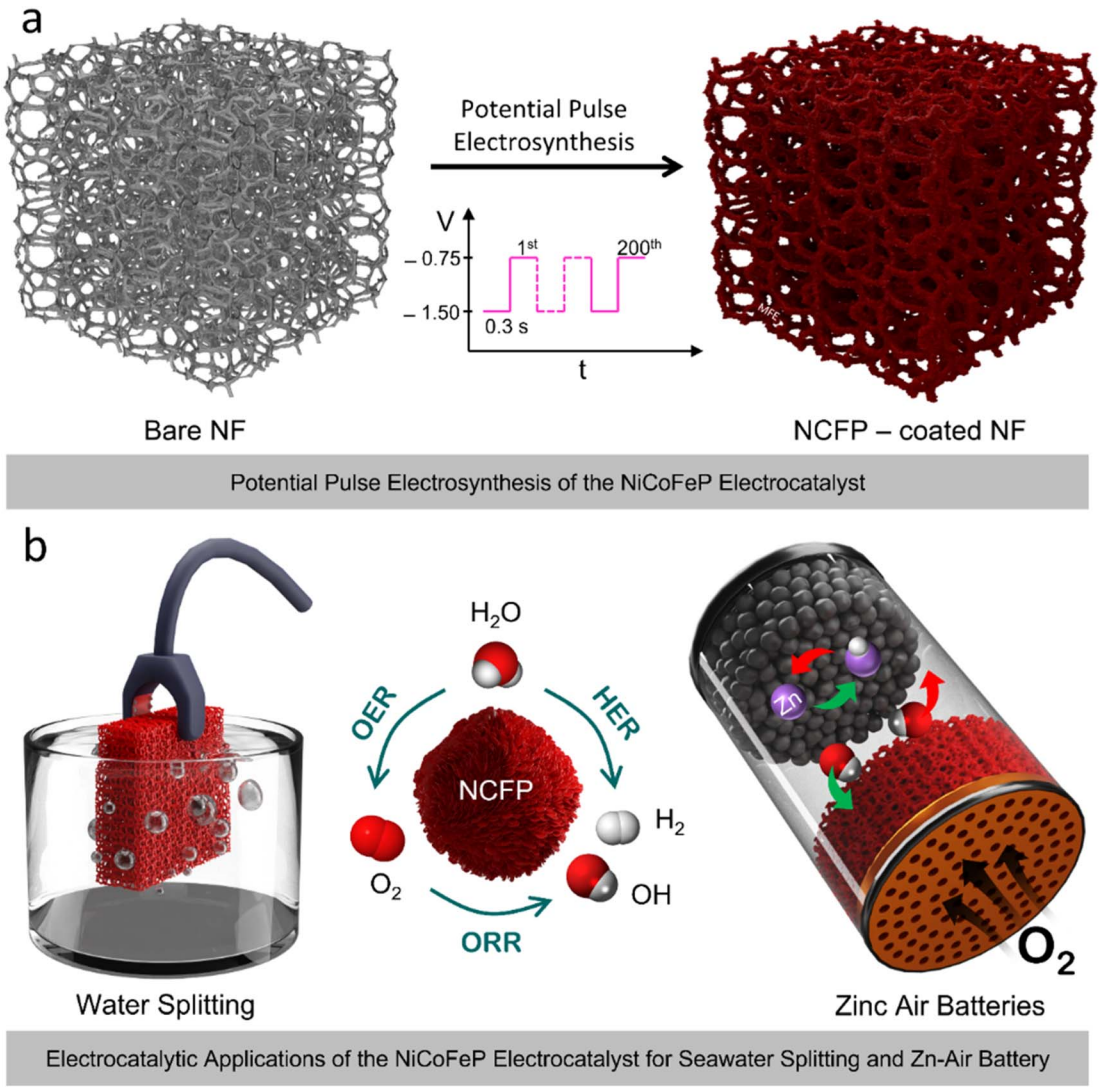

Fig. 1 Schematic illustration of the electrosynthesis of the NCFP electrocatalyst and its applications. (a) Electrosynthesis of the NCFP electrocatalyst that lasts for just 2 min (see inset) (b) illustration of the practical application of the multifunctional NCFP electrocatalyst for overall (sea) water splitting and zinc–air batteries.

electrode (3E) cell setup in which a double-junction Ag/AgCl/Sat. KCl was used as a reference electrode, a platinum plate served as a counter electrode, and the electrocatalyst-deposited Ni foam (1.0 × 1.0 cm^2) was used as a working electrode. All of the potentials, collected with reference to a double junction Ag/AgCl/sat. KCl in the 3E cell setups, were converted to a reversible hydrogen electrode (RHE) scale, where $E_{RHE} = E_{Ag/AgCl} + 0.197\ V + 0.059\ pH$. Hydrodynamic voltammetry to study the ORR using a rotating disk electrode (RDE) or rotating ring-disk electrode (RRDE) was carried out using a Princeton Applied Research Instrument model 636A Electrode Rotator (supplied by Ametek) connected to an Autolab PGSTAT30 Potentiostat/Galvanostat (Eco-Chemie, The Netherlands) and controlled *via* Nova 2.1.4 software. The area of the glassy carbon (GC) RDE was 0.159 cm^2, and the RRDE electrode consists of a GC disc of 0.198 cm^2 and a GC ring with an internal diameter of 6.0 mm and an external diameter of 8.1 mm. In the RRDE studies, a potential of 1.05 V *vs.* RHE was applied to the ring electrode. Electrochemical impedance spectroscopy (EIS) studies were carried out over an alternative voltage amplitude of 5 mV by sweeping the AC frequency from 1 kHz to 10 mHz and the experimental data were fit using Zfit in EC-Lab software. A Solartron 1470A multichannel battery test unit (Solartron Analytical, UK) equipped with Cell Test software (v. 3.5.0) was used for the durability study of the catalytic activities and cycle stability tests. All the electrochemical studies were conducted at room temperature.

Electrosynthesis of NCFP

The NCFP electrocatalyst was electrosynthesized at room temperature in a typical three-electrode cell setup comprising a piece of Ni foam (1 × 1 cm^2) pre-treated using a HCl (1.0 M) solution as a working electrode, platinum plate as a counter electrode, and Ag/AgCl as a reference electrode. The

electrosynthesis solution consists of $NiCl_2 \cdot 6H_2O$ (0.05 M), $CoCl_2 \cdot 6H_2O$ (0.05 M), and $FeCl_3 \cdot 6H_2O$ (0.05 M) as well as CH_3COONa (0.2 M) (pH ~4.5–5.5), as a buffer to maintain pH stability[37] and NaCl (0.1 M) as a supporting electrolyte to enhance ionic conductivity. Prior to the electrosynthesis process, $NaH_2PO_2 \cdot H_2O$ (0.2 M) as a green phosphorus precursor was added to the above mixture and stirred for 2 h. Note that the sum of the molarities of the metallic species (Ni^{II}, Co^{II}, Fe^{III}) was lower than that of phosphorus. The electrosynthesis process was conducted *via* a potential pulse technique that involved applying two cathodic potential pulses; an optimized nucleation potential pulse of −1.5 V for 0.3 s, followed by a growth potential pulse of −0.75 V for 0.3 s. These double potential step pulses were repeated for 200 cycles (2.0 min) to provide a mass loading of ~2 mg cm^{-2}.

HER/OER/ORR measurements

The electrocatalytic HER/OER performances of the electrocatalysts were studied by recording the linear sweep voltammetry (LSV) curves in a KOH (1.0 M) electrolyte at a scan rate of 1 mV s^{-1}. The overall water/seawater splitting process was conducted in a two-electrode cell made from the NCFP1 electrocatalyst as the cathode and the NCFP2 electrocatalyst as the anode (NCFP1(−)||NCFP2(+)). The ORR studies were conducted in a standard three-electrode cell setup with a glassy carbon (GC, 0.159 cm^2) rotating disk electrode (RDE) in a KOH (0.1 M) electrolyte. To prepare the RDE, 0.5 mg of the electrodeposited NCFP film was carefully scratched off from the Ni foam, mixed with 2 mg of carbon black and 15 μL of Nafion (5 wt%), and dispersed in 485 μL of ethanol. Then, the mixture was sonicated in an ultrasonic bath to obtain a homogeneous catalyst ink. The prepared catalyst ink contains 20 wt% NCFP2 to ensure comparability with typical standard catalysts. The as-prepared catalyst ink (10 μL) was finally drop-cast onto the surface of a pre-cleaned GC RDE (mass loading = 0.31 mg cm^{-2}) and dried at room temperature. For comparison, a mixture of commercial 20 wt% Pt/C, RuO_2, and carbon black were prepared in the same way.

Methods for detecting OCl^-

To check the selectivity of the electrocatalyst towards the desired HER and OER processes, the possible formation of Cl_2 was checked using an o-Tolidine indicator. The o-Tolidine indicator was prepared by dissolving 0.1 g o-Toluidine in 15 mL of concentrated hydrochloric acid, followed by diluting the solution to 100 mL with DI water. 200 μL of electrolyte that underwent the OER was taken out from the seawater splitting cell, mixed with 600 μL of o-Toluidine indicator solution and 200 μL of 0.5 M H_2SO_4. The changes in the color of the solution from colorless to yellow, when ClO^- is present, was monitored using UV-vis spectroscopy at a wavelength of 437 nm.

Zn–air battery assembly and electrochemical test

The homemade parallel plate aqueous Zn–air battery (ZAB) was fabricated using Zn coarse powder as a negative electrode (thickness ≤0.35 mm). The positive electrode was a piece of Ni foam (NF) one side of which was coated with the electrodeposited NCFP film or Pt/C + RuO_2 and its other side was coated by ~10 mg of a gas-diffusion layer (GDL) (thickness ≤0.45 mm). Note that during the NCFP electrodeposition process, the electrocatalyst is also slightly electrosynthesized on the second side of the NF substrate. The GDL slurry was prepared by dispersing active carbon and carbon black (CB) in 100 μL of ethanol solution containing 10 μL of PTFE (40 wt%). After drying, the air cathode was pressed at 50 kg cm^{-2} and the total thickness of the cathode was 0.45 mm. The electrolyte was a KOH (6.0 M) solution containing $Zn(OAC)_2$ (0.2 M) as an additive, and a cellulosic paper or Celgard M824 was utilized as a separator. In order to assemble a quasi-solid-state flexible Zn–air battery, a piece of flexible Zn foil (0.1 mm) was used as an anode, the same air cathode as outlined previously was used as a cathode, and a PVA-in-KOH gel containing $Zn(OAC)_2$ was utilized as an electrolyte, with no need for a separator. The $Zn(OAC)_2$-containing solid-state PVA-in-KOH electrolyte was prepared by dissolving PVA powder (1.0 g, M_w = 72 000) in 10 mL of deionized water at 90 °C under stirring for 2 h. Next, 1.0 mL of KOH (18 M) containing zinc acetate (0.2 M) was added and stirred at 95 °C for an additional 1 h. Then the gel was poured into a Petri dish and frozen at −20 °C for 12 h to obtain the solid-state $Zn(OAC)_2$-incorporated PVA-in-KOH film. Before using it as a solid-state electrolyte, the film was thawed to room temperature and dipped into KOH (6.0 M). Finally, the NCFP/NF/GDL air electrode and Zn foil were attached to the two sides of the gel electrolyte film (1 × 1 cm^2), and then two pieces of laminate paper (flexible acrylic tape) were used to seal the solid-state Zn–air battery.

Results and discussion

Microscopic and spectroscopic characterizations

Tuning of the texture, surface morphology, and interfacial properties of the electrocatalysts significantly affect their electrocatalytic activities.[38–40] Under optimized conditions (see ESI Fig. S1–S6†), the resulting NCFP catalyst (either NCFP1 as the best performing HER electrocatalyst or NCFP2 as the best electrocatalyst for the OER) displayed a 3D porous texture. The NCFP1 particles display a vertically aligned and interconnected nanowall morphology (Fig. S7†), whereas the NCFP2 particles exhibit a spherical morphology with worm-like nanostructures (~30 nm diameter) (Fig. 2a–c). The morphological differences observed between as-synthesized NCFP1 and NCFP2 are attributed to variations in Fe content, which likely influence the preferential growth facets, thereby leading to distinct morphological shapes. The porous worm-like morphology (preserved after long-term operation, Fig. S8†) not only facilitates the transport of ions into and out of the material, but also provides large, accessible active sites for catalytic activity.[41] Constituent elements of the NCFP electrode and a homogeneous distribution of them were determined using an FE-SEM-energy dispersive X-ray spectroscope, EDS (Fig. S9–S11, ESI†). Bright field TEM verified the highly porous nature of the NCFP2 catalyst, showing well-resolved fibrils arranged into discrete networks (Fig. 2d–f). This 3D hierarchical texture benefits fast ion

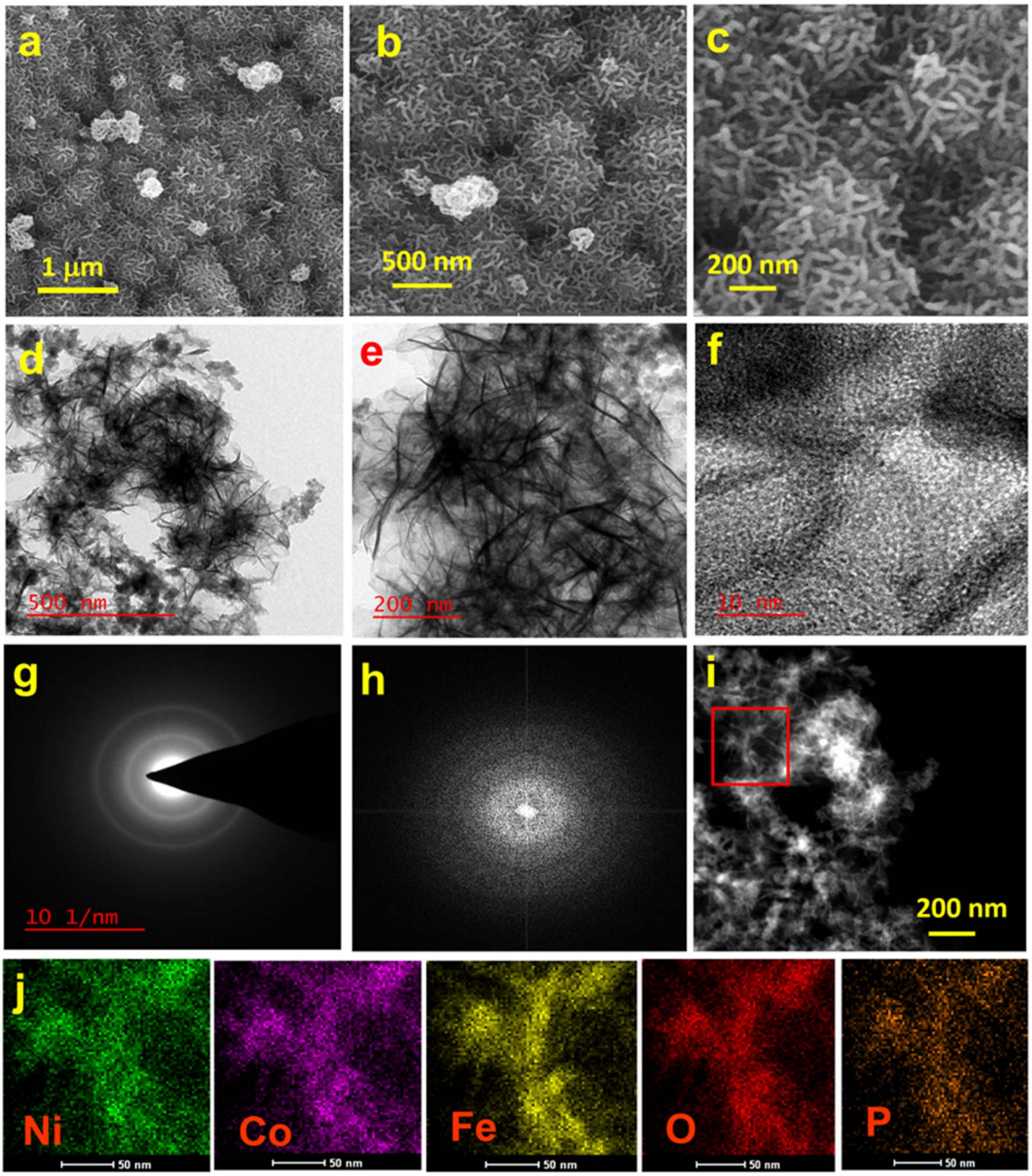

Fig. 2 Electron microscopic characterization of the NCFP catalyst. (a–c) The FE-SEM images of the catalyst at different magnifications. (d and e) The bright field TEM images of the catalyst. (f) The high-resolution TEM image, (g) the SAED pattern, and (h) the FFT image of the NCFP catalyst. (i) The HAADF-STEM image and (j) the corresponding elemental mapping of Ni, Co, Fe, O, and P elements.

transport, active site accessibility, and ultrafast escape of the H_2 and O_2 bubbles. The HR-TEM image without lattice fringes (Fig. 2f), along with the electron diffraction ring pattern of the SAED (Fig. 2g) that was further complemented with an FFT image (Fig. 2h) revealed the fully amorphous nature of the NCFP catalyst. The HAADF-STEM image and the corresponding high spatial resolution elemental mapping confirm the uniform distribution of the Ni, Co, Fe, P, and O elements throughout the catalyst (Fig. 2i and j).

The powder X-ray diffraction (XRD) pattern of the as-synthesized NCFP2 catalyst (similar to NCFP1) displayed a broad peak at $2\theta = 45.91°$ (Fig. 3a), which represents irregularities in the periodic distribution of the atoms, and implies its amorphous nature.

The survey X-ray photoelectron spectroscopy (XPS) spectrum of the NCFP2 catalyst (Fig. 3b) indicates the formation of a metal phosphide that contains some oxidized species as well. The high-resolution spectrum of Ni 2p suggests that Ni is in its +2 oxidation state, attributed to Ni–P.[42] The peaks at the binding

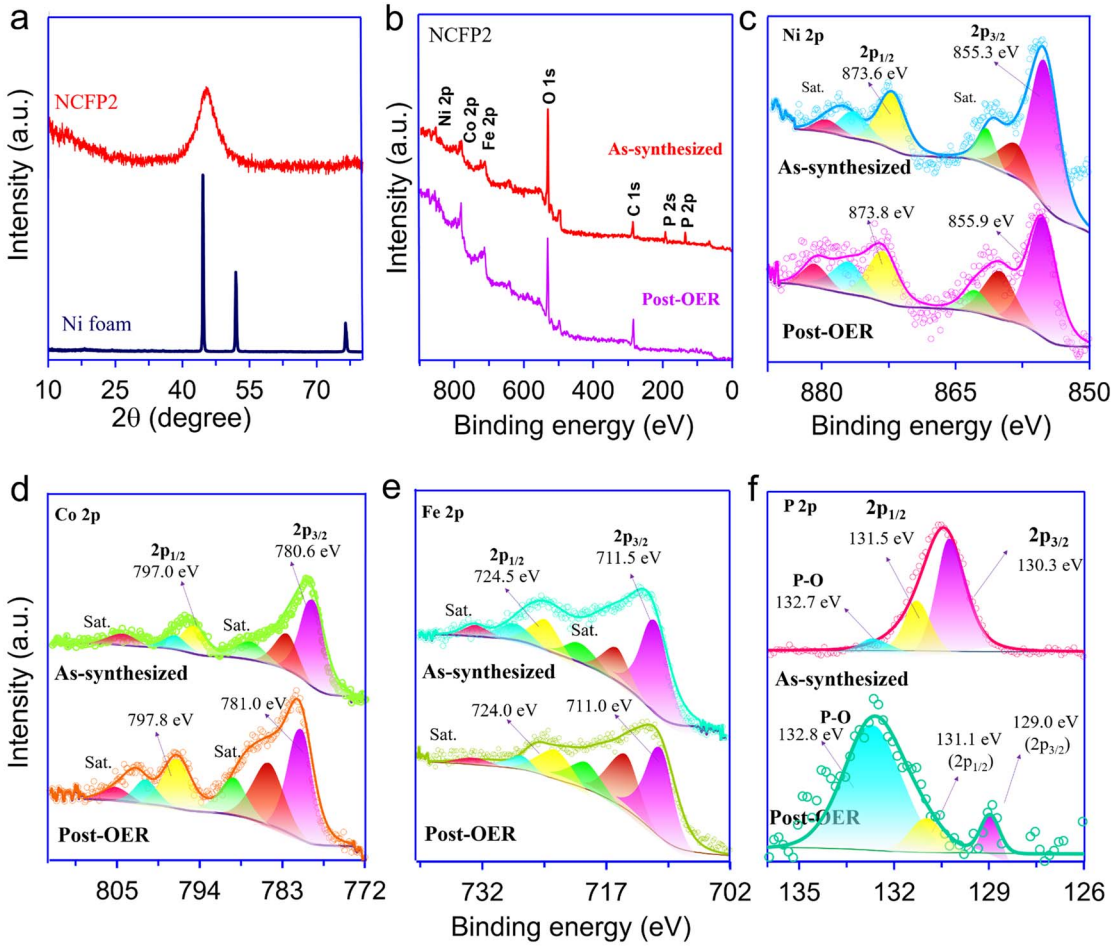

Fig. 3 Spectroscopic characterization of the NCFP catalyst. (a) XRD patterns of the bare Ni foam and the NCFP catalyst scratched off from the Ni foam substrate. (b) The survey XPS spectra of the NCFP catalysts before and after the OER. High-resolution XPS spectra of (c) Ni 2p, (d) Co 2p, (e) Fe 2p, as well as (f) P 2p before (top) and after (bottom) the OER operation.

energies of 857.0 and 874.8 eV are related to $NiPO_x$ (Fig. 3c).[43] The XPS spectrum of Co 2p can be deconvoluted into four components: the first doublet at 780.6 eV and 797.0 eV can be assigned to Co^{3+} $2p_{3/2}$ and Co^{3+} $2p_{1/2}$, and the second doublet at 782.8 eV and 798.2 eV can be ascribed to the splitting peaks of Co^{2+} $2p_{3/2}$ and Co^{2+} $2p_{1/2}$, confirming the Co–P and Co–P–O bonds (Fig. 3d).[44] The peaks of Fe species appear as Fe^{2+} $2p_{3/2}$ at 711.57 eV (Fe–P), Fe^{2+} $2p_{1/2}$ at 724.5 eV (Fe–P–O), Fe^{3+} $2p_{3/2}$ at 715 eV, and Fe^{3+} $2p_{1/2}$ at 728 eV (Fe–P–O) (Fig. 3e).[45–48] The high-resolution spectrum of P 2p exhibits two main peaks at binding energies of 130.3 ($2p_{3/2}$) and 131.5 eV ($2p_{1/2}$) (Fig. 3f), confirming the metal phosphide formation (Fig. 3f).[44] The low-intense peak located at 132.7 eV is attributed to the surface-oxidized phosphorus species; the strong hydrophilic property of which enhances the intimate contact between the electrocatalyst and the electrolyte.

TMPs undergo a phase transformation from metal phosphide precatalysts to metal oxides/(oxy)hydroxides, which are true catalysts under the OER condition.[49] To reveal this structural change, the XPS spectra of the NCFP electrocatalysts were also recorded after the OER/HER operation (Fig. 3c–f, bottom spectra), the detailed discussion of which can be found in the ESI (Fig. S12 and S13).† Comparison of the spectra for as-synthesized and post-OER electrocatalysts reveals an increase in the area under the deconvoluted peaks for M^{3+} species relative to M^{2+} states. This suggests partial oxidation of M^{2+} to higher oxidation states, forming oxides or oxyhydroxides under the oxidative OER environment. Higher-valent metal species play a key role in the OER process by stabilizing reactive oxygen intermediates like *OH, *O, and *OOH, which are critical for facilitating the oxygen evolution. The empirical formulas of the pristine and post-operational NCFP1 and NCFP2 electrocatalysts, obtained from FE-SEM-EDS (indicating the subsurface composition) and XPS (implying the surface composition), are summarized in Table S1,† indicating P is preferentially leached out of the electrocatalyst surface under long-term operation.

Electrochemical studies

OER and HER studies. Prior to electrochemical studies, the as-synthesized NCFP catalysts were activated *via* cyclic voltammetry (CV) treatment in a KOH (1.0 M) solution. The NCFP2 catalyst displays the highest activity toward the OER with the lowest overpotential of 250 ± 3 mV to attain a current density of

10 mA cm^{-2} without *iR* drop compensation (Fig. 4a), which is even lower than that of the RuO_2 benchmark electrocatalyst (η_{10} = 265 mV). Interestingly, at a high current density of 100 mA cm^{-2}, the superiority of NCFP2 (η_{100} = 299 mV) over RuO_2 (η_{100} = 356 mV) becomes more pronounced. Fig. 4b shows that the 20 wt% Pt/C, a benchmark HER catalyst, renders the best HER catalytic performance ($\eta_{10} \approx 0$ mV). Even though Pt ranks at the top of the HER electrocatalyst, the HER activity of the NCFP1 catalyst (η_{10} = 102 ± 2 mV) classifies it among the most promising alternatives to Pt noble metal (Table S2†). NCFP2 shows a low Tafel slope of 34.1 ± 2.1 mV dec^{-1} (Fig. 4c and S14†), which is far lower than that of RuO_2 (62.8 mV dec^{-1}), demonstrating that the formation of $MOOH_{ads}$ is likely the rate-determining step.[50,51] For the HER, the Tafel slope of 46.2 ± 1.3 mV dec^{-1} for NCFP1 indicates that the evolution process mostly follows through the Heyrovsky step (Volmer–Heyrovsky mechanism).[52] The ECSA value of NCFP2 was 77.9 cm^2, NCFP1 177.3 cm^2, and that of RuO_2 was 14.2 cm^2, indicating the better intrinsic catalytic activity of NCFP (Fig. S15†). Furthermore, the mass-normalized (a_{mass}) and ECSA-normalized (a_{ECSA}) activities

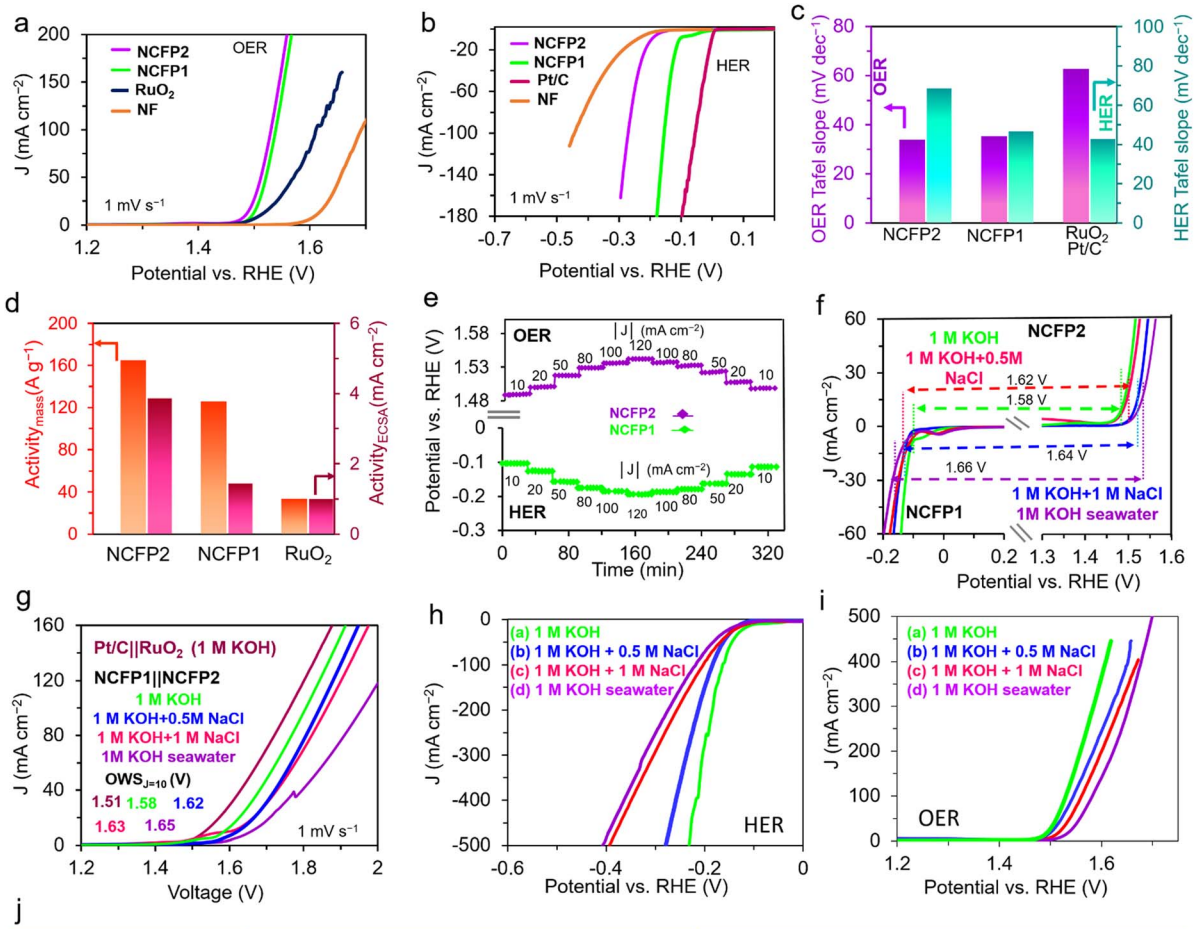

j

J (mA cm^{-2})	η_{HER} (mV)					η_{OER} (mV)				
	−100	−200	−300	−400	−500	100	200	300	400	500
1.0 M KOH	174	196	215	227	235	300	330	354	375	-
1.0 M KOH + 0.5 M NaCl	181	210	234	255	277	313	353	390	420	-
1.0 M KOH + 1.0 M NaCl	205	255	302	348	396	330	370	407	440	-
1.0 M KOH seawater	224	281	328	368	404	352	392	424	447	467

Fig. 4 The OER, HER, and OWS electrocatalytic activities of the as-prepared electrocatalysts. The LSV curves for the (a) OER and (b) HER activities of the NCFP catalysts along with the RuO_2 or Pt/C benchmark catalysts as well as the bare Ni foam in a 1.0 M KOH electrolyte at a scan rate of 1.0 mV s^{-1}. (c) The OER and HER Tafel slopes of the catalysts extracted from the LSV curves, presented in panels (a and b). (d) Mass-normalized activity (a_{mass}), ECSA-normalized activity (a_{ECSA}), and (e) rate capability studies of the NCFP2 and NCFP1 electrocatalysts using a multi-step constant current technique at different current densities from ±10 to ±120 mA cm^{-2} and back to ±10 mA cm^{-2} with a duration of 30 min at each step. (f) Overall OER and HER polarization curves of the NCFP catalysts at four different types of electrolytes: freshwater (1.0 M KOH), synthetic seawater (1.0 M KOH + 0.5 M NaCl), highly salty electrolyte (1.0 M KOH + 1.0 M NaCl), and alkaline seawater (1.0 M KOH + seawater) in three-electrode cell setups. (g) The LSV polarization curves of the NCFP1||NCFP2 and Pt/C||RuO_2 cells at a scan rate of 1.0 mV s^{-1} in the aforementioned four different types of electrolytes. (h) The HER and (i) OER polarization curves of the NCFP1 catalyst in different electrolytes, and (j) the extracted overpotentials (without *iR* compensation) at different rates from ±100 up to ±500 mA cm^{-2}.

of NCFP2 were calculated as 165.17 A g^{-1} and 3.86 mA cm^{-2}, and those of NCFP1 and RuO_2 were obtained as a_{mass}^{NCFP1} = 125.97 A g^{-1}, a_{ECSA}^{NCFP1} = 1.45 mA cm^{-2} and $a_{mass}^{RuO_2}$ = 33.63 A g^{-1}, $a_{ECSA}^{RuO_2}$ = 1.0 mA cm^{-2} at an overpotential of 350 mV, respectively (Fig. 4d). The turnover frequency (TOF) for NCFP2 at the OER overpotential of 270 mV was 0.96 s^{-1} and that of NCFP1 at the HER overpotential of 140 mV was 0.76 s^{-1} (Fig. S16†). The low Tafel slope along with the high ECSA and TOF clearly indicates the fast electrocatalytic kinetics of the NCFP catalysts. The OER (HER) electrocatalysts also demonstrate a fast response to the changes in the current densities even at a high rate of 120 (−120) mA cm^{-2} (Fig. 4e). The NCFP electrocatalysts also preserved >99.7% of the initial output voltage obtained at a rate of 10 (−10) mA cm^{-2} after 320 min of continuous OER (HER) operation at different rates and finally back to 10 (−10) mA cm^{-2}. Moreover, the long-term OER (HER) durability studies indicate that the increments in potential are only ∼3.0% and 1.8% after 300 h of OER and HER operations, respectively (Fig. S17†). The long-term stability and durability of the amorphous NCFP electrocatalysts are attributed to their remarkable self-healing and self-reconstruction capabilities. These properties allow the electrocatalysts to adapt to evolving catalytic conditions, effectively redistribute stress, and recover from operational damage. Such attributes make them highly promising candidates for applications demanding prolonged stability and reliable performance.

For a viable practical application, a high geometric catalytic activity along with a high electrical conductivity (Fig. S18†) is needed. The number of active sites per geometric area can be increased by increasing the mass loading of the catalyst and/or by nanostructuring. The big challenge is that as the mass loading increases, the intrinsic activity per site often diminishes, owing to ohmic losses and mass transport limitations. Thus, a key advantage of a synthesis strategy can be that it does not lead to the formation of a compact and thick layer of the catalyst with blocked ion penetration and electron transport pathways.[53,54] The NCFP2 electrodes with mass loadings of 2.0, 5.0, and 14.0 mg cm^{-2} displayed overpotentials of 250, 264, and 272 mV at a current density of 10 mA cm^{-2}, respectively (Fig. S19†). However, interestingly, the HER activity of the NCFP1 catalyst got better with increasing mass loading. The electrode with a mass loading of 18.7 mg cm^{-2} exhibited an overpotential of 86 mV, 18 mV less than that obtained with a mass loading of 2.0 mg cm^{-2}. It is likely that we are dealing with a different surface/interface chemistry for the catalyst with a higher mass loading (see ESI†). The high rate capability and fast response time of the high mass-loaded electrocatalyst, and the electrochemical impedance spectroscopy (EIS) studies at the OER/HER overpotentials are presented in the ESI (Fig. S20 and 21).†

Overall (sea)water splitting. Given the excellent catalytic performance of the NCFP1 and NCFP2 electrocatalysts toward the HER and OER processes, an overall water/seawater splitting cell, NCFP1(−)‖NCFP2(+), was assembled. For comparison, the control water electrolyzer cell comprised of Pt/C(−)‖RuO_2(+) was also fabricated. The NCFP-based electrocatalysts present excellent water splitting activity ($\Delta E_{OER\text{-}HER}$ = 1.58 V) that is only slightly higher than that of Pt/C‖RuO_2 electrolyzer ($\Delta E_{OER\text{-}HER}$ = 1.51 V), though the excellence of the Pt catalytic activity toward HER is undisputed (Fig. 4f–g and S22a†). These results demonstrate that water electrolysis using the NCFP1‖NCFP2 electrolyzer could be powered by a single AA battery with a nominal voltage of ≈1.5 V.

The applicability of the NCFP1‖NCFP2 electrolyzer for seawater splitting was also studied (Fig. 4g). The HER and OER catalytic activities of NCFP1 and NCFP2 were evaluated in different electrolytes: alkaline water (1.0 M KOH), synthetic seawater (0.5 M NaCl + 1.0 M KOH), highly salty electrolyte (1.0 M NaCl + 1.0 M KOH), and alkaline seawater (1.0 M KOH-added seawater). The trends of the HER and OER overpotentials and $\Delta E_{OER\text{-}HER}$ at a rate of 10 mA cm^{-2} were as follow: alkaline water ($\eta_{j=10}^{OER}$ = 250 mV, $\eta_{j=10}^{HER}$ = 102 mV, ΔE = 1.58 V) < synthetic seawater ($\eta_{j=10}^{OER}$ = 260 mV, $\eta_{j=10}^{HER}$ = 130 mV, ΔE = 1.62 V) < highly salty electrolyte ($\eta_{j=10}^{OER}$ = 285 mV, $\eta_{j=10}^{HER}$ = 125 mV, ΔE = 1.64 V) < alkaline seawater ($\eta_{j=10}^{OER}$ = 295 mV, $\eta_{j=10}^{HER}$ = 131 mV, ΔE = 1.66 V) (Fig. 4f). These performance characteristics are superior to or at least comparable with those of other electrocatalysts reported in the literature (Table S3†). Additionally, the faradaic efficiencies (FE) during the overall water splitting in 1.0 M KOH, were almost 100% for both O_2 and H_2 production (Fig. S23†). We also measured the FE% of the prototype NCFP1‖NCFP2 electrolyzer in an alkaline seawater, and confirmed it using o-Tolidine as an indicator at different time intervals.[55] The FE% was almost 100%, elucidating that the seawater splitting process is chlorine-free (see ESI for details, Fig. S24 and S25†). The rate capability studies of the NCFP1‖NCFP2 electrolyzer shows that the potential remains constant at each potential step during the 2 h study. The potential promptly jumps to a new value with an increment of current density. In contrast, for the Pt/C‖RuO_2 cell, neither the potential remains constant during each current rate nor does the electrolyzer respond quickly to the increment of the current density (Fig. S22b†). More importantly, the voltage of the NCFP1‖NCFP2 cell increased by only 5% compared to the initial voltage after 150 h of continuous overall water splitting, which was much better than that of the Pt/C‖RuO_2 cell that displayed a 17% increment in voltage (Fig. S22†). Interestingly, the NCFP1‖NCFP2 cell displayed excellent durability in a highly salty alkaline electrolyte (1.0 M KOH + 1.0 M NaCl), the potential of which increased by 10% over 150 h of continuous water splitting operation (Fig. S22c†). The HER and OER LSV curves and corresponding overpotentials in different alkaline electrolytes, up to an industrially-relevant current density of ±500 mA cm^{-2} are presented in Fig. 4h–j.

We were keen to provide descriptive information about the mechanism of the NCFP electrocatalytic activities using a theoretical method such as density functional theory (DFT). Unfortunately, reliable theoretical studies cannot be performed on amorphous materials with no long-range crystalline order. This is especially challenging for the NCFP electrocatalysts for which different arrangements of elements are possible from their empirical formula. Nevertheless, taking inspiration from the mechanisms reported for crystalline metal phosphides counterparts, it can be postulated that P (δ^-) functions as a proton

(H^+) acceptor, and transition metals (δ^+) serve as hydride (H^-) acceptors to weaken the M–H bond.[56] In an alkaline electrolyte, the concentration of protons is exceedingly low, thus, the Volmer step (formation of M–H* intermediate) is critically important for the HER catalysis. Importantly, Ni/Co/Fe-containing materials have a large number of unpaired d-orbital electrons, which tend to form chemical adsorption bonds with H*. This strong proton-accepting characteristic of the TMPs could trigger the dissociation of the water molecules, and subsequently lead to the evolution of hydrogen. Interestingly, P atoms attract electrons from the metals to promote hydrogen desorption. Thus, the coexistence of TM and P balances the Gibbs free energy change for H* adsorption to approach zero, enhancing the HER efficiency.[52,56–58]

For OER electrocatalysis, the TMP precatalyst undergoes structural and phase transformation to form the OER true catalyst.[59] This phase transformation involves partial dissolution of P and vacancy formation, enhancing the OER catalytic capability through M–O bonding of reaction intermediates. The transition metal oxide true catalysts are likely oxidized to metal oxyhydroxide (MOOH) species, which lose protons to generate MO–O peroxo intermediates, eventually breaking M–O bond to release O_2.[60–62] In general, P atoms tune the electronic structure of the metallic active sites, improving charge transport and creating a relatively larger number of valence electrons.[20,63–65] Such a P-induced electronic rearrangement triggers favorable adsorption of the reaction intermediates. In addition to electronic effects, the high electrocatalytic activity of the developed materials can also be ascribed to their structural effects. The fabricated defect-rich amorphous TMP increases the contact area between the catalytic active sites and H_2O/OH^- reactants and promotes electrocatalytic activity. The synergistic effects among the constituent elements also significantly boost its catalytic capability, as demonstrated by control experiments on monometallic and bimetallic Ni/Co/Fe phosphides (ESI, Fig. S26 and Table S4†). Potential-dependent *in situ* Raman studies were carried out to gain a deeper understanding of the dynamical processes during the HER and the OER (Fig. 5). Notably, the Raman spectrum of the pristine electrocatalysts exhibits a sharp peak at 480 cm^{-1} that can be attributed to the M–P (M = Ni, Co, Fe) bonds. Upon immersion of the pristine NCFP electrocatalyst into KOH electrolyte, the intensity of the 480 cm^{-1} peak slightly decreased, while a broad shoulder centered at around 700–900 cm^{-1} emerged, corresponding to the symmetric stretching mode of P–OH.[66–68] During the HER, as the potential decreased from 0 to −1.20 V *vs.* Ag/AgCl, the intensity of the 480 cm^{-1} peak gradually increased, albeit with minor variations (Fig. 5a). Conversely, the broad shoulder centered at higher wavenumbers slightly faded away (Fig. 5b). These observations indicate that the genuine metal phosphide phase is largely preserved during the HER process, with only minor variations experienced by the NCFP electrocatalyst. In the process toward OER, the Raman spectrum of the electrocatalyst displayed a sharp peak at 480 cm^{-1} along with a broad shoulder centered around 700–900 cm^{-1} upon immersion into KOH electrolyte (Fig. 5c). As the applied potential was increased during the OER process, the intensity of the 480 cm^{-1} peak and the 700–900 cm^{-1} shoulder remained nearly constant. However, two additional features emerged: a shoulder at 400–500 cm^{-1} (attributed to M–O bending vibration, E_g) and another at 500–600 cm^{-1} (associated with M–O stretching vibration, A_{1g}).[69,70] These new features intensified as the potential approaches 0.5 V *vs.* Ag/AgCl. It seems that, during the OER, the NCFP2 phase rapidly transformed into metal hydroxide and/or oxyhydroxide phases.[71–73] However, as the potential was increased beyond 0.5 V, the two previously emerged shoulders in the 400–600 cm^{-1} range faded away (Fig. 5d), suggesting the breakage of the M–O bond in M–O–O peroxo intermediate and release of O_2. This phenomenon has been observed in transition metal-based electrocatalysts, where oxyhydroxide-related Raman signals diminish at high anodic potentials due to bond cleavage and the subsequent evolution of oxygen.[73,74] The diminution of the peaks at potentials beyond 0.5 V can also be attributed to the interference of the Raman laser with O_2 bubbles as the OER became more severe.[75] Raman characterization of the structural stability is provided in the ESI (Fig. S27).† The *in situ* Raman spectra corroborate the results obtained from XPS characterization of both the pristine and post-OER electrocatalyst and accord well with the essential role of peroxo complex formation as previously reported for crystalline TMP electrocatalysts.[76] FT-IR characterization of the pristine NCFP2 electrocatalyst and the one after applying potential of 0.6 V *vs.* Ag/AgCl provide additional evidence that metal phosphide precatalyst converts to metal (oxy)hydroxide/oxides true catalyst under operation (see ESI, Fig. S28†). To validate the electrochemical reconstruction and get a deep understanding about reaction kinetics during the OER process, *operando* EIS studies were performed (ESI, Fig. S29 and Table S5†).

Due to the amorphous nature of the NCFP electrocatalysts and their structural transformation during OER operation, additional structural information was inferred from X-ray absorption spectroscopy (XAS), including both X-ray absorption near edge structure (XANES) and extended X-ray absorption fine structure (EXAFS). Fig. 6a–c show the XANES spectra of the as-synthesized and post-OER NCFP2 at the Ni, Co, and Fe K-edges, respectively. Comparing the XANES spectra of the as-synthesized and post-OER NCFP2 electrocatalysts at the Ni, Co, and Fe K-edges reveals an increase in the unoccupied states in the d orbitals.[27] The increase in the valence state of Ni and Fe is more pronounced than that of Co, indicating that Ni and Fe likely undergo more severe structural changes during the OER process. Considering the position of the absorption edges of the Ni foil (Ni^0), Co foil (Co^0), and Fe foil (Fe^0), as well as the NiO (Ni^{2+}), CoO (Co^{2+}), and Fe_2O_3 (Fe^{3+}) reference samples, it can be inferred that the average valence state of metal centers in NCFP2 is slightly lower than +2.[71] To gain deeper insights into the coordination environment of the Ni, Co, and Fe atoms within the as-synthesized and post-OER samples, the Fourier transformed (FT) EXAFS spectra were recorded. Fig. 6d–f illustrate the FT-EXAFS spectra of the NCFP2 electrocatalyst along with metal foils and metal oxide reference samples at the Ni, Co, and Fe K-edges. The spectrum of the as-synthesized electrocatalyst at the Ni K-edge displays one peaks at 2.23 Å, which can be attributed to the presence of Ni–P moiety; the spectrum at

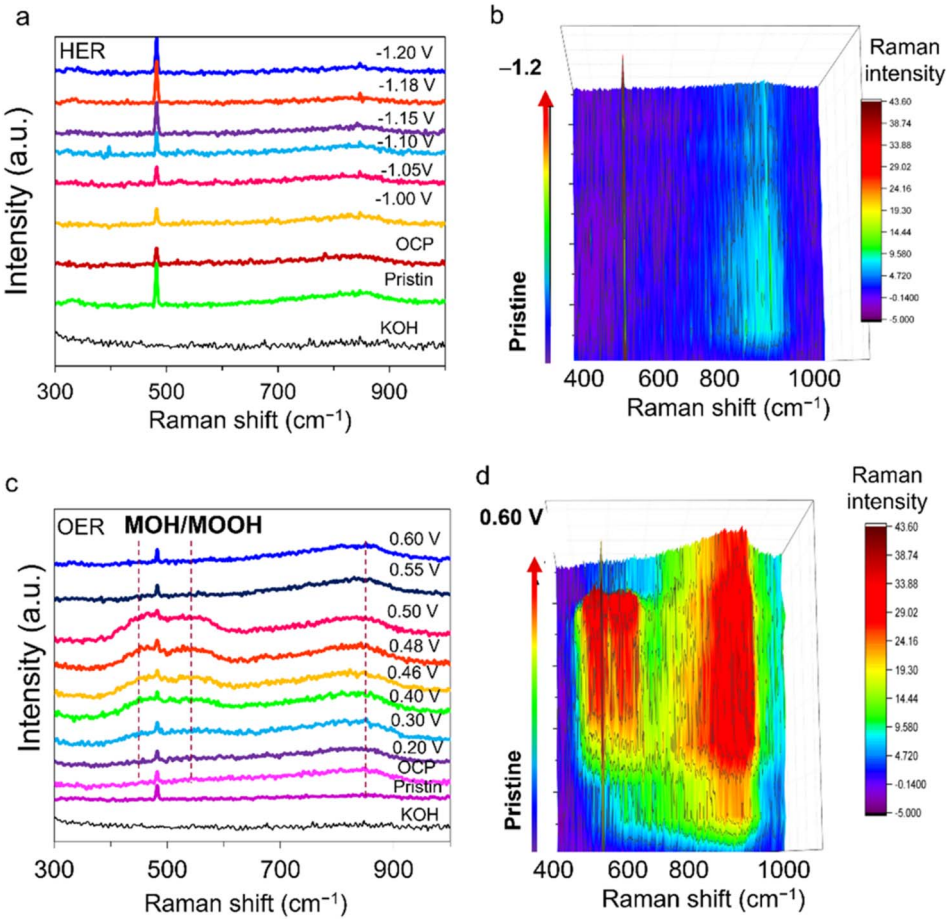

Fig. 5 *In situ* Raman measurements of NCFP electrocatalysts. The stacked *in situ* Raman spectra (left) and the corresponding contour plots (right) of the NCFP electrocatalysts in a 1.0 M KOH electrolyte during the (a and b) HER. and (c and d) OER. All potentials are referenced against an Ag/AgCl electrode.

the Co K-edge displays two peaks at 2.18, and 3.00 Å, which can be assigned to the presence of Co–P and Co–Co(Fe) moieties; and the spectrum at the Fe K-edge displays two peaks at 1.97 and 2.91 Å, which can be ascribed to the presence of Fe–P and Fe–Fe(Co) moieties, respectively. The spectra of the post-OER electrocatalyst at the Ni K-edge and Co K-edge preserve the M–P and M–M moieties, although their intensities are changed; and the spectrum at the Fe K-edge shows two peaks at 2.48 and 3.22 Å, which can be ascribed to Fe–P and Fe–Fe bonds.[77–80] The bonding characteristics were further validated using wavelet transform (WT) analysis (Fig. 6g–i). We fit the recorded EXAFS spectra of the as-synthesized and post-OER electrocatalysts in *R*-space with the spectra of various metal phosphide standards (Fig. 6j–l and Table S6†). For the as-synthesized NCFP2 electrocatalyst, the Ni K-edge EXAFS spectrum in *R*-space fits well with Ni_3P in the first coordination shell (Fig. 6j, top), and the coordination number of Ni is ~3 (refer to Table S6† for the precise fit values). Similarly, the Co K-edge fitting in *R*-space shows a good match with Co_2P, with a coordination number of ~3 for Co (Fig. 6k, top), and the Fe K-edge fitting aligns with Fe_2P, with a coordination number of 4 for Fe (Fig. 6l, top). However, the scenario for the post-OER electrocatalyst differs slightly. The Ni K-edge EXAFS spectrum of the post-OER electrocatalyst in *R*-space still fits well with the Ni_3P path in the first coordination shell, but the coordination number of Ni increases to 5 (Fig. 6j, bottom). The Co K-edge spectrum fits with CoP, showing a coordination number of ~4 for Co (Fig. 6k, bottom), and the Fe K-edge spectrum fits with Fe_3P, with an Fe coordination number of ~5 (Fig. 6l, bottom). The increase in the coordination number of metallic species in the post-OER electrocatalysts as corroborated by the experimental data, provides indirect yet significant evidence supporting the potential transformation of NCFP into higher-valent metal oxides or oxyhydroxides (M^{3+} and MOOH) during the OER process. The absence of strong spectral shifts in XAS to confirm metal oxide/oxyhydroxide formation could be attributed to several factors: (i) partial conversion of the precatalyst, rather than bulk transformation; (ii) the formation of amorphous or highly disordered oxyhydroxides, which may result in diffuse or indistinct spectral features; and (iii) a dynamic equilibrium wherein the oxyhydroxide layer forms only under applied potential and reverts to a less oxidized or intermediate state upon removal from the electrochemical environment.[59,81] Consequently, the bulk-sensitive EXAFS technique may not

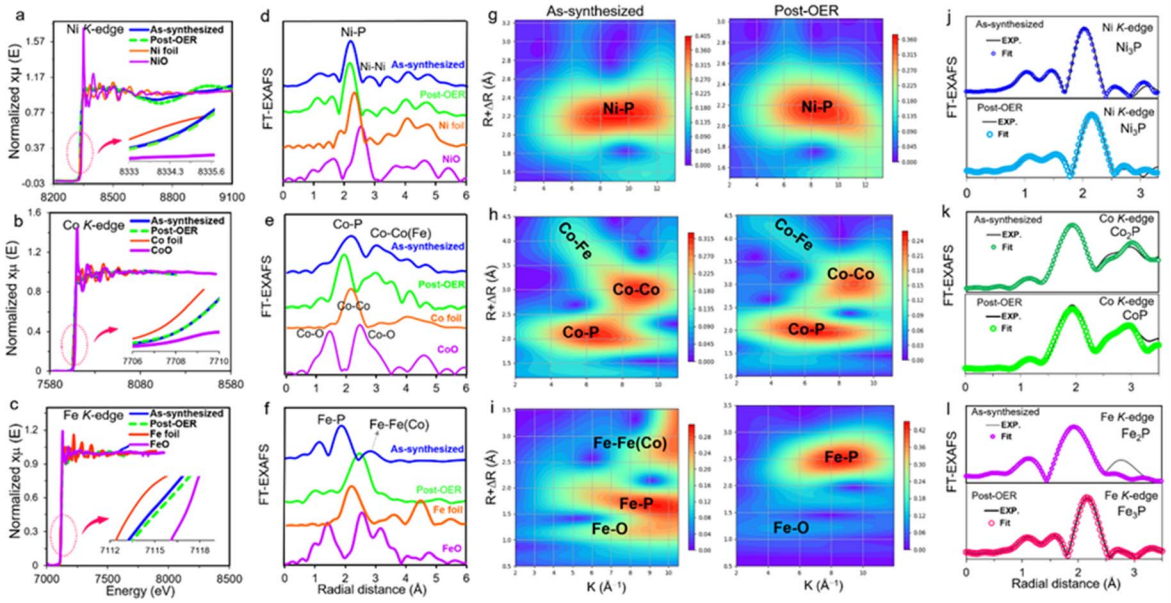

Fig. 6 XAS characterization of the as-synthesized and post-OER NCFP2 electrocatalyst. Normalized XANES spectra of the NCFP2 electrocatalyst along with metal foils and metal oxide reference samples at (a) Ni K-edge, (b) Co K-edge, and (c) Fe K-edge. The k^2-weighted FT-EXAFS spectra of the NCFP2 electrocatalyst along with metal foils and metal oxide reference samples at (d) Ni K-edge, (e) Co K-edge, and (f) Fe K-edge. WT contour plots of the as-synthesized (left) and post-OER electrocatalyst (right) at (g) Ni K-edge, (h) Co K-edge, and (i) Fe K-edge. (j–l) Fitting the EXAFS spectra of the as-synthesized (top) and post-OER (bottom) electrocatalysts to the standard metal phosphides at the (j) Ni K-edge (k) Co K-edge, and (l) Fe K-edge, and determining the coordination number.

prominently detect these surface changes, particularly if the reconstructed layer is thin.

ORR studies. The catalytic activity of the NCFP catalysts toward ORR was investigated alongside their OER activity, highlighting their potential for use in metal–air batteries. Characteristic CVs and hydrodynamic voltammograms of the electrocatalysts are presented in ESI (Fig. S30–S32 and Table S7).† The electron transfer number (n) and H_2O_2 formation were computed from the current generated on the disk and ring of a rotating ring-disk electrode (Fig. 7a). The number of electrons exchanged per O_2 molecule for NCFP1, NCFP2, and Pt/C were 3.53, 3.98, and 3.99, respectively, with an H_2O_2 yield of <2%, suggesting a nearly $4e^-$ reduction pathway (Fig. 7b). The excellent durability, outstanding methanol tolerance effect, and synergistic effects among the constituent elements of NCFP are presented in ESI (Fig. S33–S35 and Table S8†).

Rechargeable Zn–air battery assembly

A zinc–air battery (ZAB) was fabricated to assess the feasibility of NCFP application in energy conversion and storage devices (Fig. 7c and d). The Zn||NCFP2 ZAB delivered an open circuit voltage (OCV) of 1.458 V, which is even slightly higher than that of the Zn||Pt/C + RuO_2 battery (1.442 V) (Fig. S36a†). Fig. 7e presents charge–discharge polarization curves and power density plots obtained from the discharge profiles of the Zn||NCFP2, Zn||Pt/C + RuO_2, and Zn_{foil}||NCFP2 ZABs (note that wherever Zn alone is used as the anode, zinc is in a powder form). As can be seen, the Zn||NCFP2 ZAB exhibits a lower charge–discharge voltage gap (V_{gap} = 0.51 V) compared to the Zn||Pt/C + RuO_2 (V_{gap} = 0.53 V) and Zn_{foil}||NCFP2 ZABs (V_{gap} = 0.57 V) at a rate of 25 mA cm^{-2}, indicating the better rechargeability of the Zn||NCFP2 ZAB. Additionally, the Zn||NCFP2 battery delivers a maximum power density of 127 mW cm^{-2}, which is significantly higher than that of the Zn_{foil}||NCFP2 (108 mW cm^{-2}) and the Zn||Pt/C + RuO_2 (93 mW cm^{-2}) batteries. The Zn||NCFP2 device delivers an outstanding specific capacity of ~747.1 mA h g_{Zn}^{-1} (based on the consumed Zn) (91.1% utilization of the theoretical capacity of Zn, 820 mA h g_{Zn}^{-1}) and a high specific energy of 915.3 W h kg_{Zn}^{-1} at a discharge rate of −10 mA cm^{-2} along with a remarkable rate capability (Fig. S36b, ESI†), whereas the Zn||Pt/C + RuO_2 ZAB displays a specific capacity of 718.2 mA h g_{Zn}^{-1} and a specific energy of 883.6 W h kg_{Zn}^{-1} at the same rate (Fig. 7f). To fabricate a flexible solid-sate ZAB, the Zn powder anode (compressed on a piece of Cu mesh) was replaced with a Zn foil and a PVA-in-KOH gel was used as an electrolyte. Fig. 7g shows that the OCV of the flexible battery is considerably high (1.426 V) and remains constant at different bending states. The prototype solid-state flexible ZAB also demonstrated excellent practical applicability (Fig. 7h, Videos S1 and S2†). Impressively, the Zn||NCFP2 battery exhibits outstanding stability for about 189 h which is ~12.5 times more durable than the Zn||Pt/C + RuO_2 device, operating stably for only 15 h (Fig. 7i). The Zn||NCFP2 battery also shows a high round-trip efficiency of 79% in its initial cycle and 63% in its final cycle after about 189 h. All these characteristics place the fabricated ZABs in a worthy place among other same-class batteries (Table S9†).

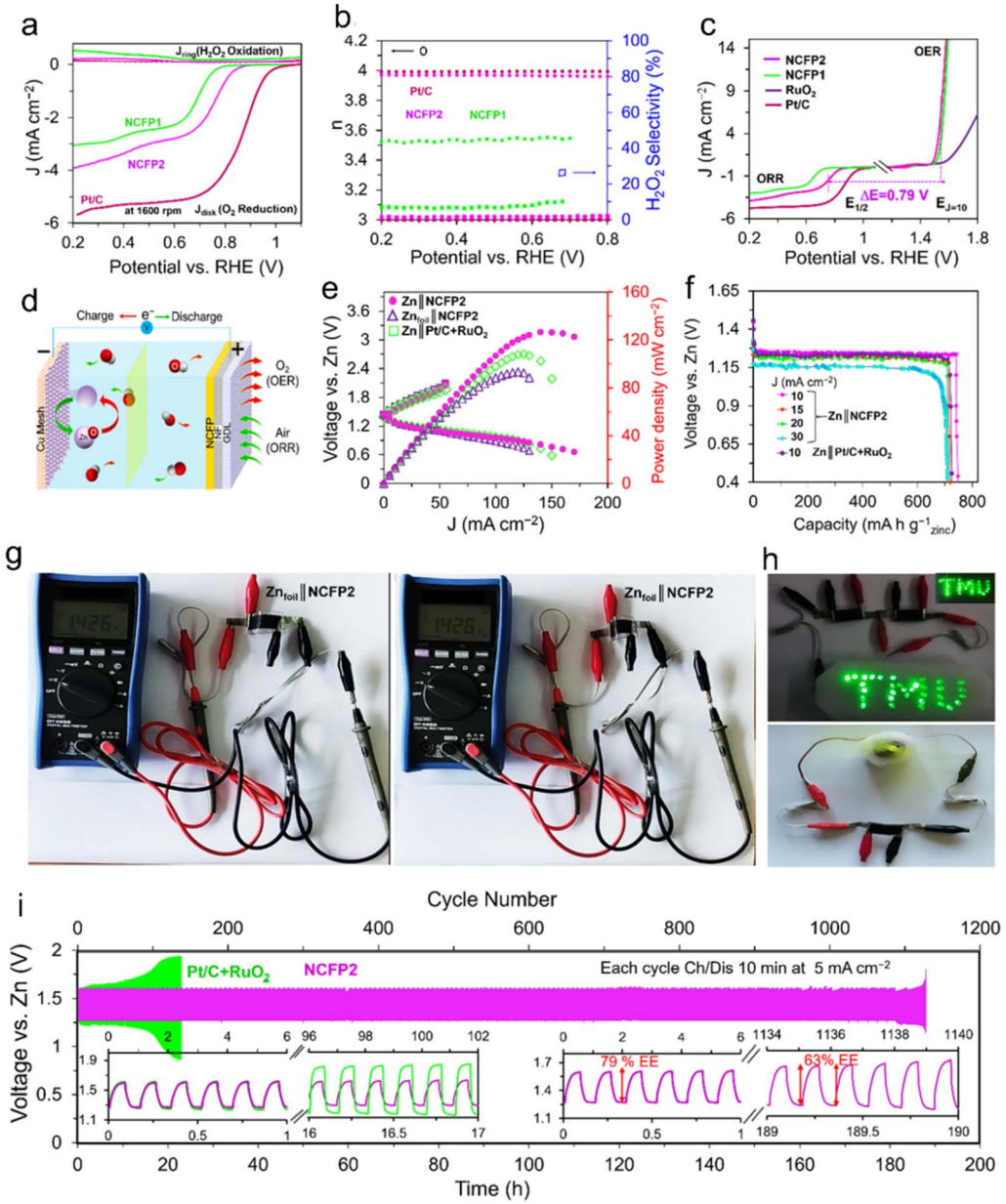

Fig. 7 The Electrocatalytic ORR/OER activities of the catalysts and their performance in Zn–air batteries. (a) Polarization curves of the as-prepared catalysts based on the RRDE results in an O_2-saturated 0.1 M KOH electrolyte at a sweep rate of 10 mV s^{-1} at 1600 rpm (the ring current was multiplied by 8 for a clear comparison between the samples). (b) Electron transfer number (n) and the H_2O_2 selectivity (%) calculated from the RRDE studies. (c) The ORR and OER polarization curves of the NCFP catalysts as well as the control samples in 0.1 M KOH at a rotation speed of 1600 rpm. (d) Schematic illustration of a Zn–air battery based on a Zn powder anode and an NCFP2 air cathode. (e) Charge and discharge curves and the corresponding power density plots of the NCFP2 and Pt/C air cathodes of Zn||NCFP2 and Zn||Pt/C + RuO_2 aqueous batteries compared with a solid-state Zn_{foil}||NCFP2 battery. (f) Discharge profiles of the Zn||NCFP2 device at different discharge current densities from 10 to 75 mA cm^{-2} and that of the Zn||Pt/C + RuO_2 device at a discharge rate of 10 mA cm^{-2}. (g) Flexibility study; monitoring the OCV of the solid-state Zn_{foil}||NCFP2 battery at different bending states. (h) Practical application of the two NCFP2-based solid-state ZABs connected in series in lighting up 33 green (2.2 V) LEDs and driving a rotor (1.0 V, 30 mW). (i) Long-term cycling performances of the ZABs based on the NCFP2 and commercial 20 wt% Pt/C + RuO_2 cathodes at a charging/discharging rate of 10 mA cm^{-2} (each cycle lasts for 10 min).

The integration of high-performance electrocatalysts in both zinc–air batteries and seawater splitting systems underscores their complementary roles in advancing renewable energy technologies. Efficient trifunctional catalysts not only enhance the oxygen evolution and reduction reactions in zinc–air batteries, boosting energy storage capabilities, but also drive water-splitting reactions for sustainable hydrogen production. This synergy enables a closed-loop energy cycle where excess renewable electricity can be stored in zinc–air batteries and later utilized to generate clean hydrogen from seawater, thus bridging energy storage and conversion for a sustainable future.

Conclusions

The Ni–Co–Fe–P amorphous electrocatalyst with outstanding trifunctional electrocatalytic activities toward the HER, OER, and ORR, and practical applications for overall seawater/water splitting and zinc–air batteries was synthesized *via* a facile and fast (2 min) potential pulse electrodeposition method. The composition, morphology, and structure of the electrocatalyst was easily tailored *via* adjusting the electrosynthesis parameters. The NCFP1 electrocatalyst displayed a low overpotential of 86 mV at a super-high mass loading of 18.7 mg cm^{-2}, indicating its viability for industrial-level hydrogen production. A water electrolyzer based on the NCFP electrocatalysts exhibited a cell voltage of 1.58 V at 10 mA cm^{-2}. The NCFP electrocatalysts also displayed excellent activity and durability in the salty aqueous samples. The figure-of-merits of the aqueous (6.0 M KOH) and quasi-solid-state (PVA-KOH gel) rechargeable Zn–air batteries were excellent compared to similar devices. These outstanding characteristics can be ascribed to: (1) the interplay of Ni, Co, and Fe in regulating the electronic properties and therefore the adsorption energies of the reaction intermediates, as well as the non-metals (P and O) that provide voids *via* dissolution. (2) The edge-enriched amorphous structure of the electrocatalyst that provides abundant active sites. (3) The unique structure of amorphous nanomaterials, optimizing the multistep reaction pathway and enhancing the intrinsic activity of each active site. (4) The amorphous multi-metal phosphide consists of different amorphous structural units simultaneously, exerting multiple structural advantages. (5) The porous structure of the electrocatalyst that facilitates ion transport and gas escape. (6) The direct electrodeposition on the conductive substrate with no need for any binder or conductive additive that minimizes contact resistance and improves the mechanical stability of the electrocatalyst under vigorous H_2/O_2 evolution.[82] (7) The larger electrochemically active surface area and the high electrical conductivity. (8) Flexibility of the amorphous electrocatalysts to adapt to new catalytic conditions. (9) Self-healing and self-reconstruction capability.[83–85] (10) The possibility to be tailored in an optimal elemental ratio with the desired catalytic performance.[86] Amorphous materials are likely to become a widely utilized electrocatalysts for various reactions.[87] This study highlights the importance of composition tuning and texture tailoring using largely overlooked electrochemical synthesis approaches *via* which excellent multifunctional electrocatalytic activity with a very promising application prospect for seawater electrolysis and metal–air batteries are guaranteed.

Data availability

The data that support the findings of this study are available from the corresponding authors upon reasonable request.

Author contributions

Conceptualization, M. M. and M. S. R.; validation, M. M., A. N., and M. S. R.; formal analysis, M. M., M. S. R., E. M., and M. V.; investigation, M. M., A. N., M. S. R.; writing – original draft, M. M., and A. N.; writing – review & editing, X. X., Y. Z., A. V., D. K., R. B. K., and M. F. M.; visualization, A. N., M. F. E., and N. B. M.; resources, X. X., Y. Z., A. V., D. K., R. B. K., and M. F. M.; funding acquisition, R. B. K. and M. F. M.; supervision, A. N., R. B. K., and M. F. M.

Conflicts of interest

There are no conflicts to declare.

Acknowledgements

This work was made possible through financial support from the Tarbiat Modares University Research Council, the Iranian National Science Foundation (INSF) under grant No. [4028746], and the Research Core of Tarbiat Modares University under grant No. [IG-39802], (M. F. M.), and the Dr Myung Ki Hong Endowed Chair in Materials Innovation at UCLA (R. B. K.). The authors greatly appreciate Dr Abharana Nagendra for conducting the XAS measurements.

Notes and references

1 D. Voiry, H. S. Shin, K. P. Loh and M. Chhowalla, Low-dimensional catalysts for hydrogen evolution and CO_2 reduction, *Nat. Rev. Chem*, 2018, **2**, 0105.
2 J.-T. Ren, L. Chen, H.-Y. Wang, W.-W. Tian and Z.-Y. Yuan, Water electrolysis for hydrogen production: from hybrid systems to self-powered/catalyzed devices, *Energy Environ. Sci.*, 2024, **17**, 49–113.
3 L. Quan, H. Jiang, G. Mei, Y. Sun and B. You, Bifunctional Electrocatalysts for Overall and Hybrid Water Splitting, *Chem. Rev.*, 2024, **124**, 3694–3812.
4 J. Liu, S. Duan, H. Shi, T. Wang, X. Yang, Y. Huang, G. Wu and Q. Li, Rationally designing efficient electrocatalysts for direct seawater splitting: challenges, achievements, and promises, *Angew. Chem.*, 2022, **134**, e202210753.
5 L. Liao, D. Li, Y. Zhang, Y. Zhang, F. Yu, L. Yang, X. Wang, D. Tang and H. Zhou, Complementary Multisite Turnover Catalysis toward Superefficient Bifunctional Seawater Splitting at Ampere-Level Current Density, *Adv. Mater.*, 2024, **36**, 2405852.
6 Y. Yu, W. Zhou, X. Zhou, J. Yuan, X. Zhang, X. Meng, F. Sun, J. Gao and G. Zhao, Taking Advantage of Activation Potential Coincidence to Unlock Stable Direct Seawater Splitting, *Adv. Funct. Mater.*, 2025, 2419871.
7 A. Ashoori, A. Noori, M. S. Rahmanifar, A. Morsali, N. Hassani, M. Neek-Amal, H. Ghasempour, X. Xia, Y. Zhang, M. F. El-Kady, R. B. Kaner and M. F. Mousavi, Tailoring Metal–Organic Frameworks and Derived Materials for High-Performance Zinc–Air and Alkaline Batteries, *ACS Appl. Mater. Interfaces*, 2023, **15**, 30220–30239.
8 X. Fan, H. Wang, X. Liu, J. Liu, N. Zhao, C. Zhong, W. Hu and J. Lu, Functionalized Nanocomposite Gel Polymer Electrolyte with Strong Alkaline-Tolerance and High Zinc Anode Stability for Ultralong-Life Flexible Zinc–Air Batteries, *Adv. Mater.*, 2023, **35**, 2209290.

9 X. Bi, Y. Jiang, R. Chen, Y. Du, Y. Zheng, R. Yang, R. Wang, J. Wang, X. Wang and Z. Chen, Rechargeable zinc–air *versus* lithium–air battery: from fundamental promises toward technological potentials, *Adv. Energy Mater.*, 2024, **14**, 2302388.

10 F. Shahbazi Farahani, M. S. Rahmanifar, A. Noori, M. F. El-Kady, N. Hassani, M. Neek-Amal, R. B. Kaner and M. F. Mousavi, Trilayer Metal–Organic Frameworks as Multifunctional Electrocatalysts for Energy Conversion and Storage Applications, *J. Am. Chem. Soc.*, 2022, **144**, 3411–3428.

11 R. F. Service, Zinc aims to beat lithium batteries at storing energy, *Science*, 2021, **372**, 890–891.

12 Y. Shabangoli, M. S. Rahmanifar, M. F. El-Kady, A. Noori, M. F. Mousavi and R. B. Kaner, An integrated electrochemical device based on earth-abundant metals for both energy storage and conversion, *Energy Storage Mater.*, 2018, **11**, 282–293.

13 Y. Zhao, D. P. Adiyeri Saseendran, C. Huang, C. A. Triana, W. R. Marks, H. Chen, H. Zhao and G. R. Patzke, Oxygen Evolution/Reduction Reaction Catalysts: From *In Situ* Monitoring and Reaction Mechanisms to Rational Design, *Chem. Rev.*, 2023, **123**, 6257–6358.

14 S. Liu, Y. Wei, M. Wang and Y. Shen, The future of alkaline water splitting from the perspective of electrocatalysts-seizing today's opportunities, *Coord. Chem. Rev.*, 2025, **522**, 216190.

15 Q. Sha, S. Wang, L. Yan, Y. Feng, Z. Zhang, S. Li, X. Guo, T. Li, H. Li, Z. Zhuang, D. Zhou, B. Liu and X. Sun, 10,000-h-stable intermittent alkaline seawater electrolysis, *Nature*, 2025, **639**, 360–367.

16 W. Shi, T. Shen, C. Xing, K. Sun, Q. Yan, W. Niu, X. Yang, J. Li, C. Wei, R. Wang, S. Fu, Y. Yang, L. Xue, J. Chen, S. Cui, X. Hu, K. Xie, X. Xu, S. Duan, Y. Xu and B. Zhang, Ultrastable supported oxygen evolution electrocatalyst formed by ripening-induced embedding, *Science*, 2025, **387**, 791–796.

17 M. Moloudi, A. Noori, M. S. Rahmanifar, Y. Shabangoli, M. F. El-Kady, N. B. Mohamed, R. B. Kaner and M. F. Mousavi, Layered Double Hydroxide Templated Synthesis of Amorphous NiCoFeB as a Multifunctional Electrocatalyst for Overall Water Splitting and Rechargeable Zinc–Air Batteries, *Adv. Energy Mater.*, 2023, **13**, 2203002.

18 D. Li, Y. Zhang, W. Xie, Q. Zhou, F. Yu, Y. Qi, Z. Lian, L. Zhang, H. Wang, D. Tang and H. Zhou, Collaborative multi-interface engineering and dynamic iron exchange boost robust bifunctional water electrolysis at 2 A cm^{-2}, *Energy Environ. Sci.*, 2025, **18**, 1320–1330.

19 T. Guo, P. Hu, L. Li, Z. Wang and L. Guo, Amorphous materials emerging as prospective electrodes for electrochemical energy storage and conversion, *Chem*, 2023, **9**, 1080–1093.

20 K. Zhang, Q. Su, W. Shi, Y. Lv, R. Zhu, Z. Wang, W. Zhao, M. Zhang, S. Ding, S. Ma, G. Du and B. Xu, Copious Dislocations Defect in Amorphous/Crystalline/Amorphous Sandwiched Structure P–$NiMoO_4$ Electrocatalyst toward Enhanced Hydrogen Evolution Reaction, *ACS Nano*, 2024, **18**, 3791–3800.

21 J. Kang, X. Yang, Q. Hu, Z. Cai, L.-M. Liu and L. Guo, Recent Progress of Amorphous Nanomaterials, *Chem. Rev.*, 2023, **123**, 8859–8941.

22 Y. Zhang, S. Jeong, E. Son, Y. Choi, S. Lee, J. M. Baik and H. Park, In Situ Phase Separation-Induced Self-Healing Catalyst for Efficient Direct Seawater Electrolysis, *ACS Nano*, 2024, **18**, 16312–16323.

23 F. Meharban, C. Lin, X. Wu, L. Tan, H. Wang, W. Hu, D. Zhou, X. Li and W. Luo, Scaling Up Stability: Navigating from Lab Insights to Robust Oxygen Evolution Electrocatalysts for Industrial Water Electrolysis, *Adv. Energy Mater.*, 2024, **14**, 2402886.

24 B. Liu, X. Lan, Q. Zhong and T. Wang, Metal Phosphide: An Atypical Catalytic Site, *ACS Catal.*, 2024, **14**, 757–775.

25 R.-Q. Li, X. Wang, S. Xie, S. Guo, Z. Cao, Z. Yan, W. Zhang and X. Wan, Vanadium-regulated nickel phosphide nanosheets for electrocatalytic sulfion upgrading and hydrogen production, *Chem. Sci.*, 2025, **16**, 809–815.

26 Y. Zhao, X. Wu, H. Wang, M. Ma, J. Tian and X. Wang, Phosphorus Regulates Coordination Number and Electronegativity of Cobalt Atomic Sites Triggering Efficient Photocatalytic Water Splitting, *Nano Lett.*, 2024, **24**, 16175–16183.

27 S. Li, L. Wang, H. Su, A. N. Hong, Y. Wang, H. Yang, L. Ge, W. Song, J. Liu, T. Ma, X. Bu and P. Feng, Electron Redistributed S-Doped Nickel Iron Phosphides Derived from One-Step Phosphatization of MOFs for Significantly Boosting Electrochemical Water Splitting, *Adv. Funct. Mater.*, 2022, **32**, 2200733.

28 D. Liu, G. Xu, H. Yang, H. Wang and B. Y. Xia, Rational Design of Transition Metal Phosphide-Based Electrocatalysts for Hydrogen Evolution, *Adv. Funct. Mater.*, 2023, **33**, 2208358.

29 S. Sun, X. Zhou, B. Cong, W. Hong and G. Chen, Tailoring the d-band centers endows $(Ni_xFe_{1-x})_2P$ nanosheets with efficient oxygen evolution catalysis, *ACS Catal.*, 2020, **10**, 9086–9097.

30 S.-H. Li, M.-Y. Qi, Z.-R. Tang and Y.-J. Xu, Nanostructured metal phosphides: from controllable synthesis to sustainable catalysis, *Chem. Soc. Rev.*, 2021, **50**, 7539–7586.

31 J. Cai, Y. Song, Y. Zang, S. Niu, Y. Wu, Y. Xie, X. Zheng, Y. Liu, Y. Lin and X. Liu, N-induced lattice contraction generally boosts the hydrogen evolution catalysis of P-rich metal phosphides, *Sci. Adv.*, 2020, **6**, eaaw8113.

32 K. Kawashima, R. A. Márquez, L. A. Smith, R. R. Vaidyula, O. A. Carrasco-Jaim, Z. Wang, Y. J. Son, C. L. Cao and C. B. Mullins, A Review of Transition Metal Boride, Carbide, Pnictide, and Chalcogenide Water Oxidation Electrocatalysts, *Chem. Rev.*, 2023, **123**, 12795–13208.

33 M. Cui, B. Xu, Y. Ding, W. Sun, H. Liu and S. Dou, Deriving multi-metal nanomaterials on metal–organic framework platforms for oxygen electrocatalysis, *Energy Environ. Sci.*, 2024, **17**, 4010–4035.

34 W. Shi, H. Liu, J. Zhang, S. Shen, Y. Wang, Y. Guo, K. Yue, Z. Liang, H. Zhang, L. Zhang, F. Tan, Z. Liang, Y. Liu,

Y. Su, D. Su, Y. Huang, B. Y. Xia and Y. Yao, Roll-to-roll synthesis of multielement heterostructured catalysts, *Nat. Synth.*, 2025, DOI: 10.1038/s44160-025-00758-y.

35 J. Zhang, X. Fu, S. Kwon, K. Chen, X. Liu, J. Yang, H. Sun, Y. Wang, T. Uchiyama, Y. Uchimoto, S. Li, Y. Li, X. Fan, G. Chen, F. Xia, J. Wu, Y. Li, Q. Yue, L. Qiao, D. Su, H. Zhou, W. A. Goddard and Y. Kang, Tantalum-stabilized ruthenium oxide electrocatalysts for industrial water electrolysis, *Science*, 2025, **387**, 48–55.

36 B. Ravel and M. Newville, ATHENA, ARTEMIS, HEPHAESTUS: data analysis for X-ray absorption spectroscopy using IFEFFIT, *J. Synchrotron Radiat.*, 2005, **12**, 537–541.

37 M. Chen, J. Qi, W. Zhang and R. Cao, Electrosynthesis of NiP_x nanospheres for electrocatalytic hydrogen evolution from a neutral aqueous solution, *Chem. Commun.*, 2017, **53**, 5507–5510.

38 S. Kogularasu, Y. Y. Lee, B. Sriram, S. F. Wang, M. George, G. P. Chang-Chien and J. K. Sheu, Unlocking catalytic potential: exploring the impact of thermal treatment on enhanced electrocatalysis of nanomaterials, *Angew. Chem.*, 2024, **136**, e202311806.

39 K. Mishra, N. Devi, S. S. Siwal and V. K. Thakur, Insight perspective on the synthesis and morphological role of the noble and non-noble metal-based electrocatalyst in fuel cell application, *Appl. Catal., B*, 2023, **334**, 122820.

40 J. Wang, Y. Sun, Y. Cui and H. Qiu, Tailored on-surface fabrication of mesoporous metallic composites by direct pyrolysis of metal ion-accumulated micellar films for enhanced electrocatalytic water splitting, *Energy Environ. Sci.*, 2025, **18**, 1756–1766.

41 K. Wang, S. He, B. Li, H. Du, T. Wang, Z. Du, L. Xie and W. Ai, Relaying alkaline hydrogen evolution over locally amorphous Ni/Co-based phosphides constructed by diffusion-limited phase-transition, *Appl. Catal., B*, 2023, **339**, 123136.

42 H. Yousefzadeh, A. Noori, M. S. Rahmanifar, N. Hassani, M. Neek-Amal, M. F. El-Kady, A. Vinu, R. B. Kaner and M. F. Mousavi, Partial Sulfidation of the Electrochemically Exfoliated Layered Double Hydroxides toward Advanced Aqueous Zinc Batteries, *Adv. Energy Mater.*, 2023, **13**, 2302137.

43 F. Hu, S. Zhu, S. Chen, Y. Li, L. Ma, T. Wu, Y. Zhang, C. Wang, C. Liu and X. Yang, Amorphous metallic NiFeP: a conductive bulk material achieving high activity for oxygen evolution reaction in both alkaline and acidic media, *Adv. Mater.*, 2017, **29**, 1606570.

44 Y. Yu, W. Zhou, X. Zhou, J. Yuan, X. Zhang, L. Wang, J. Li, X. Meng, F. Sun, J. Gao and G. Zhao, The Corrosive Cl^--Induced Rapid Surface Reconstruction of Amorphous NiFeCoP Enables Efficient Seawater Splitting, *ACS Catal.*, 2024, **14**, 18322–18332.

45 X. F. Lu, L. Yu and X. W. Lou, Highly crystalline Ni-doped FeP/carbon hollow nanorods as all-pH efficient and durable hydrogen evolving electrocatalysts, *Sci. Adv.*, 2019, **5**, eaav6009.

46 F. Yu, H. Zhou, Y. Huang, J. Sun, F. Qin, J. Bao, W. A. Goddard, S. Chen and Z. Ren, High-performance bifunctional porous non-noble metal phosphide catalyst for overall water splitting, *Nat. Commun.*, 2018, **9**, 1–9.

47 Y. Yu, J. Ma, C. Chen, Y. Fu, Y. Wang, K. Li, Y. Liao, L. Zheng and X. Zuo, General Method for Synthesis Transition-Metal Phosphide/Nitrogen and Phosphide Doped Carbon Materials with Yolk-Shell Structure for Oxygen Reduction Reaction, *ChemCatChem*, 2019, **11**, 1722–1731.

48 N. Khodayar, A. Noori, M. S. Rahmanifar, Y. Shabangoli, A. Baghervand, M. F. El-Kady, N. Hassani, X. Chang, M. Neek-Amal, R. B. Kaner and M. F. Mousavi, Super-Fast and Super-Long-Life Rechargeable Zinc Battery, *Adv. Energy Mater.*, 2022, **12**, 2202784.

49 J. Song, Are Metal Chalcogenides, Nitrides, and Phosphides Oxygen Evolution Catalysts or Bifunctional Catalysts?, *ACS Energy Lett.*, 2017, **2**, 1937–1938.

50 X. Xie, L. Du, L. Yan, S. Park, Y. Qiu, J. Sokolowski, W. Wang and Y. Shao, Oxygen Evolution Reaction in Alkaline Environment: Material Challenges and Solutions, *Adv. Funct. Mater.*, 2022, **32**, 2110036.

51 A. Moysiadou, S. Lee, C.-S. Hsu, H. M. Chen and X. Hu, Mechanism of Oxygen Evolution Catalyzed by Cobalt Oxyhydroxide: Cobalt Superoxide Species as a Key Intermediate and Dioxygen Release as a Rate-Determining Step, *J. Am. Chem. Soc.*, 2020, **142**, 11901–11914.

52 K. Bhunia, M. Chandra, S. K. Sharma, D. Pradhan and S.-J. Kim, A critical review on transition metal phosphide based catalyst for electrochemical hydrogen evolution reaction: Gibbs free energy, composition, stability, and true identity of active site, *Coord. Chem. Rev.*, 2023, **478**, 214956.

53 W. Xie, Z. Li, S. Jiang, J. Li, M. Shao and M. Wei, Mass-loading independent electrocatalyst with high performance for oxygen reduction reaction and Zn-air battery based on Co-N-codoped carbon nanotube assembled microspheres, *Chem. Eng. J.*, 2019, **373**, 734–743.

54 N. Khodayar, A. Noori, M. S. Rahmanifar, M. Moloudi, N. Hassani, M. Neek-Amal, M. F. El-Kady, N. B. Mohamed, X. Xia, Y. Zhang, R. B. Kaner and M. F. Mousavi, An ultra-high mass-loading transition metal phosphide electrocatalyst for efficient water splitting and ultra-durable zinc–air batteries, *Energy Environ. Sci.*, 2024, **17**, 5200–5215.

55 J. Li, Y. Liu, H. Chen, Z. Zhang and X. Zou, Design of a Multilayered Oxygen-Evolution Electrode with High Catalytic Activity and Corrosion Resistance for Saline Water Splitting, *Adv. Funct. Mater.*, 2021, **31**, 2101820.

56 L. K. Putri, B.-J. Ng, R. Y. Z. Yeo, W.-J. Ong, A. R. Mohamed and S.-P. Chai, Engineering nickel phosphides for electrocatalytic hydrogen evolution: A doping perspective, *Chem. Eng. J.*, 2023, **461**, 141845.

57 R. B. Wexler, J. M. P. Martirez and A. M. Rappe, Active role of phosphorus in the hydrogen evolving activity of nickel phosphide (0001) surfaces, *ACS Catal.*, 2017, **7**, 7718–7725.

58 K. Wang, X. She, S. Chen, H. Liu, D. Li, Y. Wang, H. Zhang, D. Yang and X. Yao, Boosting hydrogen evolution *via*

optimized hydrogen adsorption at the interface of CoP_3 and Ni $_2$P, *J. Mater. Chem. A*, 2018, **6**, 5560–5565.

59 J. Han, J. Sun, S. Chen, S. Zhang, L. Qi, A. Husile and J. Guan, Structure–Activity Relationships in Oxygen Electrocatalysis, *Adv. Mater.*, 2024, **36**, 2408139.

60 J. Liu and L. Guo, In situ self-reconstruction inducing amorphous species: A key to electrocatalysis, *Matter*, 2021, **4**, 2850–2873.

61 C.-J. Huang, H.-M. Xu, T.-Y. Shuai, Q.-N. Zhan, Z.-J. Zhang and G.-R. Li, A review of modulation strategies for improving catalytic performance of transition metal phosphides for oxygen evolution reaction, *Appl. Catal., B*, 2022, **325**, 122313.

62 C. Guan, W. Xiao, H. Wu, X. Liu, W. Zang, H. Zhang, J. Ding, Y. P. Feng, S. J. Pennycook and J. Wang, Hollow Mo-doped CoP nanoarrays for efficient overall water splitting, *Nano Energy*, 2018, **48**, 73–80.

63 L. Yi, Y. Zhang, K. Nie, B. Li, Y. Yuan, Z. Liu and W. Huang, Recent advances in the engineering and electrochemical applications of amorphous-based nanomaterials: A comprehensive review, *Coord. Chem. Rev.*, 2024, **501**, 215569.

64 Y. Gao, H. Liang, H. Xu, D. Cui, C. Wu, J. Chen, Y. Liu, S.-x. Dou, W. Huang and L. Lin, Emerging Amorphized Metastable Structures to Break Limitations of 2D Materials for More Promising Electrocatalysis, *ACS Energy Lett.*, 2024, **9**, 3982–4002.

65 J. Kang, F. Li, Z. Xu, X. Chen, M. Sun, Y. Li, X. Yang and L. Guo, How Amorphous Nanomaterials Enhanced Electrocatalytic, SERS, and Mechanical Properties, *JACS Au*, 2023, **3**, 2660–2676.

66 S. El Makhloufy, E. M. Majdi, A. Ouasri, S. Chtita, M. Saadi, L. E. Ammari, A. Cherqaoui and S. Belaaouad, Synthesis, crystal structure, IR, Raman-spectroscopy and DFT computation of monostrontium phosphate monohydrate, Sr $(H_2PO_4)_2 \cdot H_2O$, *J. Coord. Chem.*, 2020, **73**, 2328–2346.

67 M. Premila, R. Rajaraman, S. Abhaya, R. Govindaraj and G. Amarendra, Atmospheric corrosion of boron doped iron phosphate glass studied by Raman spectroscopy, *J. Non-Cryst. Solids*, 2020, **530**, 119748.

68 J. Conrad and P. R. Tremaine, Third dissociation constant of phosphoric acid in H_2O and D_2O from 75 to 300 °C at p= 20.4 MPa using Raman spectroscopy and a titanium-sapphire flow cell, *Phys. Chem. Chem. Phys.*, 2021, **23**, 10670–10685.

69 W. Liu, Z. Liang, S. Jing, J. Zhong, N. Liu, B. Liao, Z. Song, Y. Huang, B. Yan and L. Gan, Asymmetrical Triatomic Sites with Long-Range Electron Coupling for Ultra-durable and Extreme-Low-Temperature Zinc-Air Batteries, *Angew. Chem., Int. Ed.*, 2025, e202503493, DOI: **10.1002/ange.202503493**.

70 J. Zhong, Z. Liang, N. Liu, Y. Xiang, B. Yan, F. Zhu, X. Xie, X. Gui, L. Gan, H. B. Yang, D. Yu, Z. Zeng and G. Yang, Engineering Symmetry-Breaking Centers and d-Orbital Modulation in Triatomic Catalysts for Zinc-Air Batteries, *ACS Nano*, 2024, **18**, 5258–5269.

71 Y. Zhao, N. Dongfang, C. A. Triana, C. Huang, R. Erni, W. Wan, J. Li, D. Stoian, L. Pan and P. Zhang, Dynamics and control of active sites in hierarchically nanostructured cobalt phosphide/chalcogenide-based electrocatalysts for water splitting, *Energy Environ. Sci.*, 2022, **15**, 727–739.

72 M. R. Kandel, U. N. Pan, P. P. Dhakal, R. B. Ghising, T. T. Nguyen, J. Zhao, N. H. Kim and J. H. Lee, Unique heterointerface engineering of Ni_2P–MnP nanosheets coupled Co_2P nanoflowers as hierarchical dual-functional electrocatalyst for highly proficient overall water-splitting, *Appl. Catal., B*, 2023, **331**, 122680.

73 X. Mu, M. Yu, X. Liu, Y. Liao, F. Chen, H. Pan, Z. Chen, S. Liu, D. Wang and S. Mu, High-Entropy Ultrathin Amorphous Metal–Organic Framework-Stabilized Ru (Mo) Dual-Atom Sites for Water Oxidation, *ACS Energy Lett.*, 2024, **9**, 5763–5770.

74 N. Yao, H. Jia, J. Zhu, Z. Shi, H. Cong, J. Ge and W. Luo, Atomically dispersed Ru oxide catalyst with lattice oxygen participation for efficient acidic water oxidation, *Chem*, 2023, **9**, 1882–1896.

75 J. Woo, J. Choi, J. Choi, M.-Y. Lee, E. Kim, S. Yun, S. Yoo, E. Lee, U. Lee, D. H. Won, J. H. Park, Y. J. Hwang, J. S. Yoo and D. K. Lee, Mechanistic Insights into the Role of Elements in Ni-Co-P Catalysts for Electrochemical Conversion of 5-Hydroxymethylfurfural to 2,5-Furandicarboxylic Acid, *Adv. Funct. Mater.*, 2024, **35**, 2413951.

76 J. Huang, Y. Li, Y. Zhang, G. Rao, C. Wu, Y. Hu, X. Wang, R. Lu, Y. Li and J. Xiong, Identification of key reversible intermediates in self-reconstructed nickel-based hybrid electrocatalysts for oxygen evolution, *Angew. Chem.*, 2019, **131**, 17619–17625.

77 Y. Luo, P. Wang, G. Zhang, S. Wu, Z. Chen, H. Ranganathan, S. Sun and Z. Shi, Mn-doped nickel–iron phosphide heterointerface nanoflowers for efficient alkaline freshwater/seawater splitting at high current densities, *Chem. Eng. J.*, 2023, **454**, 140061.

78 S. Ramakrishnan, D. B. Velusamy, S. Sengodan, G. Nagaraju, D. H. Kim, A. R. Kim and D. J. Yoo, Rational design of multifunctional electrocatalyst: An approach towards efficient overall water splitting and rechargeable flexible solid-state zinc–air battery, *Appl. Catal., B*, 2022, **300**, 120752.

79 H. Sun, Y. Min, W. Yang, Y. Lian, L. Lin, K. Feng, Z. Deng, M. Chen, J. Zhong, L. Xu and Y. Peng, Morphological and Electronic Tuning of Ni_2P through Iron Doping toward Highly Efficient Water Splitting, *ACS Catal.*, 2019, **9**, 8882–8892.

80 M. H. Al Rashid, A. L. Dipu, Y. Nishikawa, H. Ogihara, Y. Inami, S. Iguchi, I. Yamanaka, S.-i. Nagamatsu, D. Kido, B. Hu and K. Asakura, X-ray absorption fine structure studies on nickel phosphide catalysts for the non-oxidative coupling of methane reaction using a theoretical model, *Radiat. Phys. Chem.*, 2021, **189**, 109727.

81 J. Feng, X. Wang and H. Pan, In-situ Reconstruction of Catalyst in Electrocatalysis, *Adv. Mater.*, 2024, **36**, 2411688.

82 X. Wang, W. Ma, C. Ding, Z. Xu, H. Wang, X. Zong and C. Li, Amorphous multi-elements electrocatalysts with tunable bifunctionality toward overall water splitting, *ACS Catal.*, 2018, **8**, 9926–9935.

83 M. Ning, S. Wang, J. Wan, Z. Xi, Q. Chen, H. Yu, Y. Sun, H. Li, T. Ma and H. Jin, Dynamic Active Sites in Electrocatalysis, *Angew. Chem.*, 2024, **136**, e202415794.
84 H. Meng, Z. Chen, J. Zhu, B. You, T. Ma, W. Wei, S. Vernuccio, J. Xu and B. J. Ni, In situ amorphization of electrocatalysts, *Adv. Funct. Mater.*, 2024, **34**, 2405270.
85 J. Wang, Controlling dynamic reconstruction chemistry for superior oxygen-evolving catalysts, *Chem*, 2023, **9**, 1645–1657.
86 T. Guo, L. Li and Z. Wang, Recent development and future perspectives of amorphous transition metal-based electrocatalysts for oxygen evolution reaction, *Adv. Energy Mater.*, 2022, **12**, 2200827.
87 C. Wan, Z. Zhang, J. Dong, M. Xu, H. Pu, D. Baumann, Z. Lin, S. Wang, J. Huang and A. H. Shah, Amorphous nickel hydroxide shell tailors local chemical environment on platinum surface for alkaline hydrogen evolution reaction, *Nat. Mater.*, 2023, **22**, 1022–1029.